

TRANSLATIONAL CHEMISTRY

AN INTERFACE JOURNAL

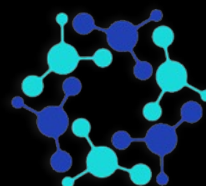


Editors in Chief

Carlos Lodeiro Y Espiño , PhD

José Luis Capelo – Martínez, PhD

Laura Mercolini, PhD



PROTEOMASS
SCIENTIFIC
SOCIETY



Translational Chemistry

An Interface Journal

EDITORIAL BOARD

Translational Chemistry Journal Editorial Board 2025

REVIEW ARTICLE

Colloidal Metallic Nanoparticles: An Introduction to Concepts and Properties

ORIGINAL ARTICLE

Smartphone-based Colorimetric Protein Quantification in Human Urine Using Gold Nanoparticles

EDITORIAL BOARD



TRANSLATIONAL CHEMISTRY

AN INTERFACE JOURNAL

[HTTPS://WWW.TRANSLATIONALCHEMISTRY.COM/](https://www.translationalchemistry.com/)



EDITORIAL BOARD | DOI: 10.5584/translationalchemistry.v1i2.246

TRANSLATIONAL CHEMISTRY AN INTERFACE JOURNAL

EDITORS-IN-CHIEF

Prof. Carlos Lodeiro

LAQV-REQUIMTE, NOVA FCT, NOVA University Lisbon, Caparica 2829-516 Portugal

Prof. Laura Mercolini

Department of Pharmacy and Biotechnology, University of Bologna, Italy

Prof. José Luis Capelo-Martínez

LAQV-REQUIMTE, NOVA FCT, NOVA University Lisbon, Caparica 2829-516 Portugal

EXECUTIVE EDITORS

Dr. Adrián Fernández-Lodeiro

Department of Electrical and Computer Engineering, University of Cyprus, Nicosia, Portugal

Prof. Elisabete Oliveira

LAQV-REQUIMTE, NOVA FCT, NOVA University Lisbon, Caparica 2829-516 Portugal

Prof. Emília Bértolo

School of Psychology and Life Sciences, Canterbury Christ Church University, UK

Prof. Hugo M. Santos

LAQV-REQUIMTE, NOVA FCT, NOVA University Lisbon, Caparica 2829-516 Portugal

Dr. Javier Fernández-Lodeiro

LAQV-REQUIMTE, NOVA FCT, NOVA University Lisbon, Caparica 2829-516 Portugal

Dr. Luís B. Carvalho

LAQV-REQUIMTE, NOVA FCT, NOVA University Lisbon, Caparica 2829-516 Portugal

Dr. Silvia Nuti

Department of Chemistry, University of Bologna, Italy

ASSOCIATED EDITORS

Prof. Ana Luísa Fernando

MEtRICs/CubicB, NOVA FCT, NOVA University Lisbon,
Caparica 2829-516 Portugal

Prof. Ana Rita Duarte

LAQV-REQUIMTE, NOVA FCT, NOVA University Lisbon,
Caparica 2829-516 Portugal

Prof. Artur Badyda

Warsaw University of Technology, Faculty of Environmental
Engineering, Poland

Prof. Atanas Kurutos

Bulgarian Academy of Sciences, Institute of Organic
Chemistry with Centre of Phytochemistry, Bulgaria

Prof. Clement Cabanetos

CNRS, University of Angers, France

Prof. Federica Pellati

University of Modena and Reggio Emilia, 41125, Modena,
Italy

Dr. Fernanda Papa Spada

University of São Paulo, Brazil

Prof. Gilberto Igrejas

University of Trás os Montes e Alto Douro, Portugal

Prof. Jakub Zdarta

Faculty of Chemical Technology, Poznan University of
Technology, Poland

Prof. Jean Christophe Pouilly

University of Caen, France

Prof. José Manuel Vila Abad

Department of Inorganic Chemistry, University of Santiago
de Compostela, Spain

Prof. Massimo La Deda

Department of Chemistry and Chemical Technology,
University of Calabria, Italy

Dr. Marco Carlotti

Dipartimento di Chimica e Chimica Industriale of the
University of Pisa, Italy

Prof. Patrícia Alexandra C.Q.D. Poeta

Veterinary and Animal Research Centre, University of Trás
os Montes e Alto Douro, Portugal

Prof. Pier Luigi Gentili

Department of Physical Chemistry - University of Perugia,
Italy

Prof. Ramón Martínez Mañez

Department of Inorganic Chemistry, Polytechnical University
of Valencia, Spain

Dr. Susana Gaudêncio

UCIBIO, NOVA FCT, NOVA University Lisbon, Caparica
2829-516 Portugal

Prof. Tarita Biver

Department of Chemistry and Industrial Chemistry -
University of Pisa, Italy

Prof. Veronica Doderio

Faculty of Chemical Technology, Poznan University of
Technology, Poland

Prof. Viviane Pilla

University of Uberlândia, Brazil

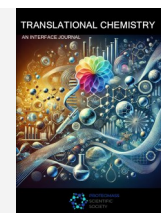
REVIEW ARTICLE



TRANSLATIONAL CHEMISTRY

AN INTERFACE JOURNAL

[HTTPS://WWW.TRANSLATIONALCHEMISTRY.COM/](https://www.translationalchemistry.com/)



REVIEW ARTICLE | DOI: 10.5584/translationalchemistry.v1i2.247

Colloidal Metallic Nanoparticles: An Introduction to Concepts and Properties

Silvia Nuti^{1,†,*}, Carlos Lodeiro^{1,2,*}

¹BIOSCOPE Research Group, LAQV-REQUIMTE, Chemistry Department, NOVA School of Science and Technology (FCT NOVA), Universidade NOVA de Lisboa, 2829-516 Caparica, Portugal. ² PROTEOMASS Scientific Society, 2825-466, Costa da Caparica, Portugal. [†] Current address: Department of Chemistry “Giacomo Ciamician”, University of Bologna, Via Gobetti 85, 40129 Bologna, Italy.

Received: 11 November 2025 **Accepted:** 22 November 2025 **Available Online:** 5 December 2025

ABSTRACT

Metallic nanoparticles (NPs) exhibit size- and shape-dependent properties that have positioned them at the forefront of nanoscience and nanotechnology. Their synthesis spans top-down and bottom-up approaches, including direct, seed-mediated, and composite strategies, each offering distinct advantages and limitations. Understanding nucleation, growth, and stabilization processes is essential to control morphology and functionality, which in turn govern their optical, catalytic, and biological behaviours. This introductory review provides a didactic overview of metallic NPs synthesis, highlighting the connection between structure and properties. Integrating historical context, theoretical principles, and practical examples, this review outlines the key concepts linking the synthesis, structure, and behaviour of metallic NPs.

Keywords: Noble metals, Nanoparticles, Synthesis, Colloids, Didactic

1. Introduction and historical perspective

Metals, such as Gold (Au), Silver (Ag), Platinum (Pt), Copper (Cu), have been used since antiquity, when they were prized for their ornamental and economic value and for their supposed healing powers [1–4]. When these materials are brought to the nanoscale range (10^{-9} m), they form structures called NP (from Ancient Greek “*vāvoc*” (nānos), meaning “*dwarf*”) which exhibit different properties when compared to the bulk metals, the most evident and captivating change is seen in the variation of the colour. Throughout history, several examples of the use of nanomaterials are reported. Cu and Ag nanocrystals were found in glazed pottery created by artisans in the Middle East in the 9th century [5]. Soluble Au was believed to have impressive curative properties, and its preparation and applications are described in two books dating back to 1618 and 1676 [6,7]. Au and Ag NPs of different sizes are the origin of the astonishing stained glass works: firstly developed in Ancient Egypt and Ancient Rome, the peak of the stained-glass windows creation was reached during the Middle Ages in the 12th century [8,9]. However, the finest example of the use of nanomaterials in antiquity is represented by the Lycurgus cup, a Roman cage cup-type vessel dating back to 4th century. Due to the presence of Au-Ag alloyed NPs, it exhibits different colour

depending on the illumination (**Figure 1**): when it is illuminated from outside, and light is reflected, it appears green, while, when it is illuminated from the inside, and the light is transmitted, the cup displays a red colour [10].



Figure 1. Lycurgus Cup (British Museum, London). When viewed in reflected light, it appears green (A). However, when the light is transmitted through the glass, it appears red (B). © The Trustees of the British Museum. Shared under a Creative Commons Attribution-NonCommercial-ShareAlike 4.0 International (CC BY-NC-SA 4.0) licence.

It was in 1857 that the observation of metallic NPs was described by the English scientist Michael Faraday in his Bakerian Lecture [11]. He was, in fact, able to obtain a ruby coloured solution and described how the colour was produced by fine particles of Au

*Corresponding author: Silvia Nuti, silvia.nuti3@unibo.it; s.nuti@campus.fct.unl.pt | Carlos Lodeiro, cle@fct.unl.pt

which are “very minute in their dimensions”, even though he could not observe them with the microscopes available at the time [12]. Almost one hundred years later, in 1951, John Turkevich and his colleagues observed the Au colloids with an electron microscope [13]. Faraday also noted that “the particles are easily rendered evident, by gathering the rays of the sun (or a lamp) into a cone by a lens, and sending the part of the cone near the focus into the fluid; the cone becomes visible, and though the illuminated particles cannot be distinguished because of their minuteness, yet the light they reflect is golden in character, and seen to be abundant in proportion to the quantity of solid gold present.”[11] observing the so-called Tyndall effect, also extensively studied in the same time frame by the Irish physicist John Tyndall.

Later on, in 1908, another important contribution to the growth of nanotechnology came from the German physicist Gustav Mie [14]. Mie theory is based on solving Maxwell's equations for electromagnetic waves interacting with a spherical particle. It describes the scattering and absorption of light by spherical particles whose size is comparable to or larger than the wavelength of the incident light and as NPs dimensions often fall within this range, the theory is particularly useful for their study. The interest towards nanotechnology and the synthesis of NPs with different composition, morphology and applications has increased significantly with a huge and constantly increasing number of documents published on this topic.

2. Synthesis of Metallic NPs

The synthesis of NPs holds immense importance in various fields of science and technology. The controlled synthesis of NPs enables researchers to tailor their size, shape, composition, and surface properties, allowing for precise manipulation of their characteristics and functionalities. Metallic NPs, with their unique physical and chemical properties, offer important opportunities for advancements in different areas such as medicine, electronics, energy, and environmental remediation.

2.1. Top-down and bottom-up approaches

The approaches for synthesising metallic NPs can be divided in two greater categories: “*top-down*” and “*bottom-up*” [15,16]. “*Top-down*” synthesis is based on the reduction of bulk materials, such as larger particles or bulk powders, to NPs through controlled mechanical, physical or chemical processes. Some of the most commonly used techniques are ball milling, mechanochemical synthesis, sputtering or laser ablation, where external forces are applied to reduce the size of the material or to induce reactions at the surface of the bulk reagents. On the other hand, “*Bottom-up*” synthesis focuses on building NPs from atomic or molecular precursors, gradually assembling them into the desired nanostructures. This approach includes many techniques in solid state (physical vapor deposition or chemical vapor deposition), liquid state (sol gel methods, chemical reduction, hydrothermal method, solvothermal method), gas phase (spray pyrolysis, laser ablation, flame pyrolysis) and other methods including biological synthesis, microwave or ultrasound techniques. One of the most

common methodologies among the “*bottom-up*” approaches is the chemical reduction method or also called wet colloidal synthesis, in which NPs are synthesized by controlling chemical reactions in a solution. This process evolves through two different phases: nucleation and growth.

2.2. Nucleation and Growth of Metallic NPs in Solution

The nucleation and growth processes are the steps involved in the colloidal synthesis of metallic NPs [17,18].

2.2.1. Nucleation

Nucleation is a thermodynamic step that leads to the formation of tiny clusters (or nuclei) from precursor species in solution. This can be initiated by, for example, the addition of a reducing agent or temperature variations. Nucleation can be distinguished by the way it occurs:

- *Heterogeneous nucleation* occurs at preferential sites such as, phase boundaries, impurities or surfaces or particles present in the system that act as nucleation sites and typically requires a lower amount of energy to be initiated.
- *Homogeneous nucleation* occurs when nuclei form spontaneously in the reaction solution. It requires a higher amount of energy together with other conditions such as supersaturation.

Nucleation is mainly explained by the Classical Nucleation Theory (CNT) [19] in which, for a spherical particle of radius r , the total free energy ΔG , is given by the sum of the surface energy γ and the free energy of the bulk crystal ΔG_v (Equation 1):

$$\Delta G = 4\pi r^2 \gamma + \frac{4}{3}\pi r^3 \Delta G_v \quad (1)$$

The free energy of the crystal, ΔG_v (Equation 2), is governed by parameters such as temperature (T), Boltzmann's constant (k_B), the supersaturation of the solution (S) and its molar volume (v) (Equation 3).

$$\Delta G_v = \frac{-k_B T \ln(S)}{v} \quad (2)$$

$$S = \frac{C_{\text{actual}} - C_{\text{equilibrium}}}{C_{\text{equilibrium}}} \quad (3)$$

Because the surface free energy is positive while the crystal free energy is negative, it is possible to find a maximum free energy corresponding to a critical cluster size. The critical radius of the nucleus identifies to the minimum size required for a particle to persist in the solution without undergoing re-dissolution. Conversely, when clusters exceed the critical radius r , growth becomes favourable (Figure 2). The critical radius is expressed as follows in Equation 4:

$$r_{\text{crit}} = -\frac{2\gamma}{\Delta G_v} \quad (4)$$

By substituting r in Equation 1 with critical radius from Equation 4 it is possible to obtain the expression for the critical free energy ΔG_c (Equation 5):

$$\Delta G_{\text{crit}} = \frac{16\pi\gamma^3}{\Delta G_v^2} \quad (5)$$

Consequently, nucleation can be promoted by increasing the supersaturation level, resulting in a reduction of the energy barrier for nucleation and raising the temperature, which increases the average atomic energy and facilitates the overcoming of critical energy or by introducing a change in surface free energy, achievable through the use of surfactants.

2.2.2. Growth

Different theories have been proposed to describe the growth of NPs following nucleation. Some theories explain the growth of NPs as atom-mediated while other as NPs-mediated. In the former, the atoms act as building blocks that aggregate on the surface of a growing nucleus, contributing to its expansion, while the latter theory involves the addition of pre-existing NPs as the fundamental units for further growth. The most representative theories are summarized below:

- *LaMer* mechanism was one of the first nucleation and growth theory to be proposed and is based on the CNT [20]. Developed for a closed system, this model describes the formation of NPs in three stages: first, an increase in the concentration of available monomers within the solution which initiates the second stage, a phenomenon called "burst nucleation," resulting in a substantial decrease of free monomers in the solution (**Figure 3**). The nucleation rate during this phase is characterized as "effectively infinite", causing minimal nucleation activity thereafter due to the diminished concentration of monomers, lastly growth continues controlled by the diffusion of monomers through the solution.
- *Ostwald and digestive ripening* are mechanisms that propose to explain the growth of NPs in solution. Ostwald ripening [21] (**Figure 4A**) occurs due to differences in solubility and surface energy between larger and smaller particles. Larger particles have

lower surface energy and are more thermodynamically stable, leading to the preferential dissolution of smaller particles and subsequent growth of larger ones. On the other hand, digestive ripening [22] (**Figure 4B**) happens when bigger NPs dissolve and the smaller ones grow. Digestive ripening can be initiated with the addition of a ligand that will help the dissolution of the bigger particles. With the equilibrium of the two process a more uniform size distribution is achieved.

- *Coalescence and Oriented attachment* are two mechanisms that explain the growth of nanocrystals as "nanoparticle-mediated growth", that occurs when smaller NPs, created in the initial stages of the reaction, merge to create bigger NPs. For *coalescence* [23] (**Figure 5**) there is no preferred merging site for the NPs that will coalesce upon contact. Conversely, for *oriented attachment* [24] (**Figure 6**) to happen, the NPs must present matching crystallographic planes. This mechanism might occur following collisions of aligned nanocrystals in suspension or when misaligned NPs will rotate towards a low-energy interface configuration.

2.3. Stability of NPs

Once NPs are synthesised, their stability in solution refers to the ability of colloidal particles to remain dispersed in a medium without aggregating or settling over time. Stability of NPs is crucial for maintaining their properties and it is also important for their further application. Multiple parameters govern colloidal stability, including van der Waals (vdW) attraction, electrostatic double-layer (EDL) repulsion, particle-size distribution, pH, temperature, surface chemistry, and steric effects [25]. vdW attractive forces (**Figure 7A**) result from the interaction of induced, instantaneous or permanent dipoles in between NPs and tend to destabilize the colloidal dispersion. These attractive forces are counteracted by electrostatic repulsion generated by the NPs EDL (**Figure 7B**).

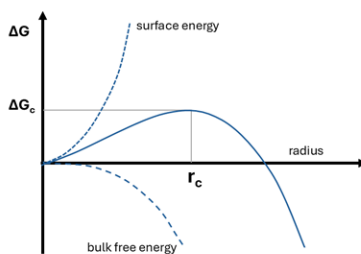


Figure 2. The dependence of the cluster free energy, on the cluster radius, according to the CNT.

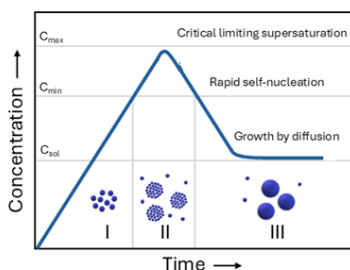


Figure 3. The principle of nanoparticle nucleation due to LaMer's mechanism of nucleation derived from CNT.

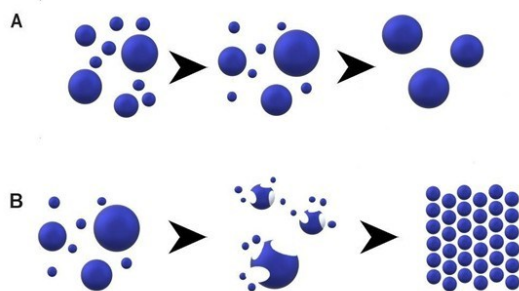


Figure 4. Representation of the (A) Ostwald ripening and (B) digestive ripening processes.

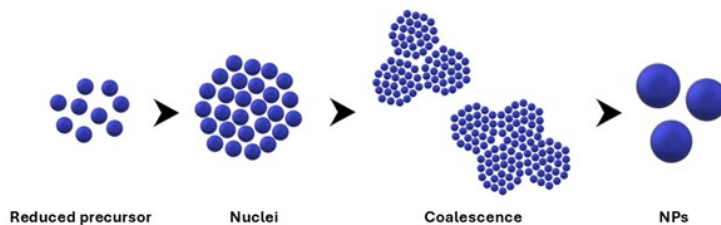


Figure 5. Representation of coalescence in the synthesis of NPs.

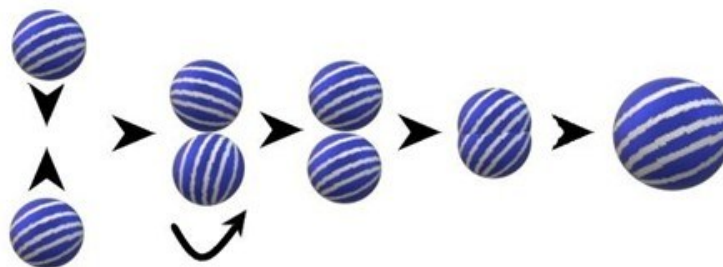


Figure 6. Representation of an oriented attached mechanism.

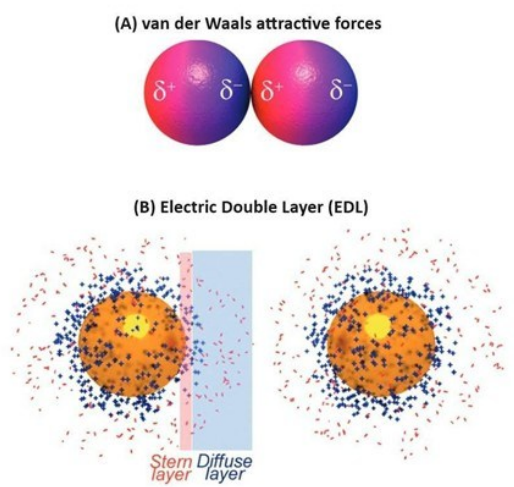


Figure 7. (A) Representation of Van der Waals interactions that can lead to nanoparticle aggregation. (B) Representation of the EDL, composed by the Stern layer and the Diffuse layer. Adapted with permission from reference [25]. Copyright 2015 Royal Society of Chemistry under a CC BY 3.0 License <https://creativecommons.org/licenses/by/3.0/>.

The EDL is formed by the Stern-layer and the diffuse layer. The surface charge of NPs, originating from surface ions or functional groups, leads to the creation of the Stern layer formed by ions with opposite charges adhering to the NP surface. The diffuse layer is formed by ions carrying a charge opposite to that of the Stern layer. The EDL results in a net charge, and when two similar particles are in proximity, the EDL causes repulsion between them. The Derjaguin–Landau–Verwey–Overbeek (DLVO) theory uses vdW forces and EDL to predict and explain NPs stability. The DLVO theory also includes contribution of pH and ionic strength of the medium. Steric stabilization (**Figure 8**), obtained through the adhesion of molecules (polymers, proteins, surfactants...) to the NPs surface, becomes a valuable tool in maintaining the dispersion of NPs, especially in challenging conditions, as it prevents the formation of attractive vdW interactions between two particles. The stability is now determined by the solubility of the molecules, average chain length, concentration or temperature. Steric stabilization will be ineffective if the obtained coating is patchy or incomplete.

2.4. Direct synthesis

Direct synthesis (also known as "one-pot") is the most straightforward method to synthesise metallic NPs in solution. This approach combines nucleation and growth happening simultaneously and in the same vessel. The metal precursor is reduced, and the newly formed NPs need to be stabilized by a capping agent present in the solution. One of the most commonly reproduced one-pot syntheses is the Turkevich synthesis. Firstly reported in 1951 [13], it involves the use of tetrachloroauric(III) acid (HAuCl_4), which is reduced and stabilized by trisodium citrate at 100 °C in water, for the preparation of spherical Au NPs with a diameter of approximately 20 nm.

Early reports of one-pot synthesis of Ag NPs, where the reduction of the metal precursor (AgNO_3) is achieved using sodium borohydride (NaBH_4) showed a less uniform size and shape distribution [26]. More recently, the one-pot synthesis of monodisperse Ag NPs, of approximately 10nm, was reported [27]. This methodology utilizes a combination of sodium citrate and tannic acid as reducing agents for AgNO_3 . It is also possible to obtain Pt NPs via a one-pot methodology [28]. In this case the reduction of the metal precursor, hexachloroplatinic acid (H_2PtCl_6) is achieved with a combination of acetylthiocholine (ATC) and NaBH_4 . While direct synthesis methodologies are popular due to their simplicity, they often lead to NPs with a spherical morphology, thus, to obtain a higher degree of control over

morphology and sizes of NPs it is necessary to resort to seed-mediate syntheses.

2.5. Seed-mediated synthesis

In seed-mediated syntheses methodologies, pre-formed particles are used as "seeds" and act as nucleation sites for the formation of the desired NPs. Typically, this methodology allows for a finer tuning of the NPs size and morphology. One of the first reported examples is the synthesis of Au nanorods [29] starting from pre-formed Au spherical seeds and utilizing cetyltrimethylammonium bromide (CTAB) as a surfactant for the formation of the rod-shaped NPs. Shortly after, the synthesis of Ag nanowires using pre-formed Pt seeds and a polyol process, was reported [30]. This approach is also applicable to spherical NPs. Starting from seeds obtained with a one-pot methodology, researchers have been able to grow Ag and Au spherical NPs [27,31] with a great control over their size distribution. Proceeding after the first step, and using the previously grown NPs as seeds, the process has been extended to several NPs generations obtaining spheres up to 200 nm. However, a greater understanding of the nature of the seeds and an appropriate choice of capping agents and surfactants, can lead to the synthesis of a broader variety of morphologies [32].

A seed can be characterized by two elements: the internal structure (or crystallinity) defined by planar defects such twin planes or stacking faults, and the surface structure (or faceting). Most noble metals crystallize in the face centred cubic (fcc) lattice, which can be explained as the stacking of closely packed, hexagonal arrays of atoms along the (111) direction.

- *Single-crystal seeds* do not present any planar defects and consists of only one single-crystal domain. They can be obtained when a strong reducing agent is used for their preparation.
- *Singly twinned seeds* present one planar defect, a (111) plane that serves as a twin boundary dividing the seed in two crystal domains. Metals such as Cu, Ag, Au often produce this type of seeds.
- *Multiply twinned seeds* are characterized by the presence of more than one twin defect. This type of seeds can be helpful in the synthesis of highly anisotropic NPs, thanks to the inhomogeneous distribution of the defects.
- *Plate-like seeds* are generated when stacking fault defects are present. The synthesis of this type of seeds is more intricate, due to the necessity of having a kinetic control over the growth of the NPs. Slow deposition of the atoms, use of mild reducing agents and the use of strong ligands are some of the favoured strategies [32].

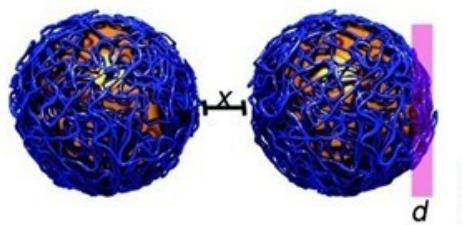


Figure 8. Representation of NPs covered with a polymer avoiding particle interaction due to steric repulsion. Adapted with permission from reference [25]. Copyright 2015 Royal Society of Chemistry under a CC BY 3.0 License <https://creativecommons.org/licenses/by/3.0/>.

Capping agents also influence the homogeneous nucleation over a pre-formed seed. Some molecules bind strongly to certain metals while other have a weaker interaction (for example, citrate will weakly bind to Au, while thiols will have a much stronger interaction). The combination between the affinity of a capping agent for a metal/specific facet will have an influence on the growth of the final NPs, as a facet that is selectively capped will be more expressed during the growth [32].

Seed-mediated protocols provide a wide range of potential morphologies beyond the nanorods and spheres mentioned earlier. Additional morphologies achievable through seed-mediated syntheses include nanoplates [33], nanocages or nanoframes [34], and branched NPs (also referred to as nanostars, nanoflowers, multipods or dendritic NPs, based on the branches number and distribution) [35]. Nanoplates represent an important class of anisotropic nanostructures distinguished by their pseudo-two-dimensional morphology with large lateral dimensions compared to thickness. One of the earliest reported examples is photoinduced method for the conversion of Ag nanospheres into triangular nanoprisms. In this process, light irradiation induces the fragmentation of spherical Ag NPs into small clusters that contribute to the growth of nanoprisms, acting as seeds, until all precursors are consumed. [36]. Around the same period truncated Ag nanoplates have been prepared through a soft-template approach using CTAB micelles [37] while PVP-assisted syntheses enabled the formation of nanoplates of other metals such as Au and Pd [37]. The formation of these plate-like structures has been associated with the presence of planar twin defects along the (111) crystallographic planes, which break the symmetry of the face-centred cubic lattice and promote two-dimensional growth. Additionally, selective ligand adsorption on specific crystal facets stabilizes the basal planes and restricts growth along the perpendicular direction, further favouring the plate morphology. One of the most striking features of this materials, when synthesised with plasmonic metals such as Au and Ag, is the possibility of tuning the LSPR band over an extensive range, from the visible to the infrared, by tuning the aspect ratio of the nanoplates by changing the synthesis conditions [38–40], making them ideal candidates for sensing applications [39].

Nanocages are a unique class of hollow nanostructures characterized by high surface-to-volume ratio, accessible inner cavities, internal and external surfaces and porous walls. They are most commonly synthesized through galvanic replacement reactions, where a less noble metal is oxidized and dissolved while a more noble metal is reduced and deposited onto its surface. In one of the first reported examples [41] Ag nanostructures were used as templates and reacted with HAuCl_4 , where Ag was oxidized to Ag^+ while Au^{3+} was reduced and deposited on the template surface, forming hollow Au shells after the complete consumption of Ag. The morphology, wall thickness, and void size of the resulting hollow structures were dictated by the size and shape of the Ag templates. This methodology was later extended to other noble metals, such as Pt and Pd, to further demonstrate the potential of this approach which was subsequently adopted for the synthesis of [42] both single- and double-shell nanocages (Au-Pt, Pt-Au, Au-Pd, Pd-Au, Pd-Pt, and Pt-Pd) via sequential galvanic replacement

steps. The optical and plasmonic characteristics of these hollow nanocages were found to depend strongly on the dielectric properties and shell thicknesses of the constituent metals. More recently, a seed-mediated method combining Pd nanocube templates, Pt-Ru deposition, and subsequent chemical etching to obtain multimetallic PdPtRu nanocages was reported [43]. The resulting nanocages exhibited open, hollow structures with tunable compositions and demonstrated significantly enhanced catalytic activity and durability. Overall, galvanic replacement and related template-mediated strategies have proven to be powerful synthetic routes for producing nanocages with controllable morphology, wall thickness, and composition. These advances have established nanocages as versatile materials for applications in catalysis, plasmonics, and energy conversion.

Branched NPs have been obtained with different metal precursors. Ag nanoflowers have been obtained from the reduction of $[\text{Ag}(\text{NH}_3)_2]^+$ by ascorbic acid, in the presence, polyvinylpyrrolidone (PVP) as stabilizer, trisodium citrate and employing single crystalline silver seeds [44]. Pd nanostars were obtained using a two-step seeded growth process, using PdCl_4^{2-} as precursor, ascorbic acid as reducing agent, CTAB as stabilizer, and copper (II) acetate to promote the anisotropic growth of different morphologies depending on its concentration [45]. For Pt, different methodologies have been reported, either using Pt seeds [46] in presence of PVP to produce single crystal NPs or Au seeds [47] to catalyse the thermal decomposition of PtCl_2 in oleylamine. Rh multipods have been prepared with the reduction of RhCl_3 in ethylene glycol in presence of PVP using Rh seeds [48].

Great research effort has been dedicated to creating branched Au NPs, thanks to their intense and highly tunable Localized surface plasmon resonance band (LSPR), enabling applications in different fields [49]. One of the first reports of Au branched NPs involved the use of PVP in dimethylformamide (DMF) both as reducing and stabilizing agent and PVP coated seeds [50]. Following the first reports on the role of AgNO_3 as shape inducing agent for the synthesis of Au nanorods [51,52], a similar methodology has been applied for the synthesis of branched Au NPs in combination with the use of surfactants such as CTAB [53,54]. The use of branched NPs in sensing and biomedical applications has been limited by the potential toxicity of surfactants like CTAB, and by the difficulty of replacing the stabilizing agents (i.e: PVP, CTAB), for further functionalization. Surfactant-free synthesis can help to advance in the bioapplication of branched NPs. Such syntheses are for example obtained with sodium citrate and hydroquinone, ascorbic acid or albumin [55–57]. Anisotropic metal NPs represent a highly versatile class of nanostructures whose design has evolved from spheres and rods to more complex morphologies such as nanoplates, nanostars, nanocages, multipods, and chiral or hierarchical architectures. The emergence of such complex architectures further illustrates the structural diversity attainable through colloidal synthesis. The ability to modulate shapes and composition at the nanoscale enables fine control of optical, catalytic, and electronic responses, supporting applications that span from SERS and chemical sensing to photocatalysis, photothermal therapy, and energy conversion [58].

2.6. Synthesis of Composite NPs

Composite NPs possess a structure comprising two or more components at the nanoscale, each exhibiting distinct physical and/or chemical properties. These components possess mutual contact interfaces, leading to a strong coupling effect on a nanometer scale. Composite NPs can combine the effects of individual components or enhance intrinsic performance and exhibit novel features, surpassing the limitations of single-component properties. Examples of composite NPs studied in this thesis work include bimetallic NPs in core@shell or alloyed morphology and metal@oxide core@shell NPs such as metallic NPs with a bulk or mesoporous silica (SiO_2) shell.

2.6.1. Bimetallic NPs

Bimetallic NPs can be synthesised in solution with similar approaches compared to their mono-metallic counterparts (“*top-down*” or “*bottom-up*” approach and direct or seed-mediated syntheses). The presence of the two metallic precursors will determine the final composition of the particles [59]. For the “*bottom-up*” approach, if the two precursors are reduced simultaneously, it is likely that the NPs will present an alloyed structure (**Figure 9A**). The two metals might be present in a statistical mixture [60] or some zones of the particles might exhibit a richer composition of one of the two metals without complete segregation [61]. Conversely, if the second metal precursor is added to a pre-formed particle (like in a seed mediated synthesis) different outcomes are possible:

- **Formation of a core@shell structure:** In this case the second metal will be reduced on the surface of the NPs creating a shell that can be continuous or patchy (**Figure 9B**).
- **Formation of a hollow structure:** This process is also referred to as “galvanic replacement” and it consists of a redox process between the pre-formed metallic NPs (sacrificial template), and metal ions

in solution. The difference in the electrical reduction potential between the sacrificial template and the metal ions in solution provides the driving force for the reaction in which the template will undergo oxidation and dissolution while the second metal ions will reduce and deposit at the surface of the template. The resulting hollow NPs will have a composition richer in the second metal. Carefully tuning the relationship between the two metal can lead to different compositions of the hollow structures (**Figure 9C**) [62,63].

Bimetallic NPs can also be synthesised through “*top-down*” methodologies, an example of this is the laser ablation method in which a bulk alloy is irradiated with a laser to obtain bimetallic NPs (**Figure 9D**) [64–66]. With this methodology it is also possible to obtain ligand-free NPs [67].

2.6.2. Noble metal@oxide core@shell NPs

Controllable integration of different materials such as noble metals (Au, Ag, Pt, and Pd) and oxides (SiO_2 , TiO_2 , CeO_2 , Cu_2O , Fe_2O_3 , ZnO , SnO_2 and ZrO_2 [68–70]) into a single nanostructure has recently become a popular research topic as these nanostructures not only combine the function of individual NPs, but also bring unique collective and synergetic properties compared with single-component materials [71]. Moreover, an oxide shell can offer extra stabilization preventing the NPs aggregation or synergetic properties when exposed to harsh conditions. Metallic NPs can be integrated in an oxide matrix in different ways such as: core–shell [72] or yolk–shell [73] structures, referring to a single noble metal core surrounded by a metal oxide shell or a single movable noble metal core inside a hollow metal oxide shell, respectively, but also multiple noble metal cores [74] coated with a metal oxide shell or sandwich structures [75] between multiple metal NPs and an oxide layer, or multiple noble metal NPs embedded [76] within metal oxide matrices.

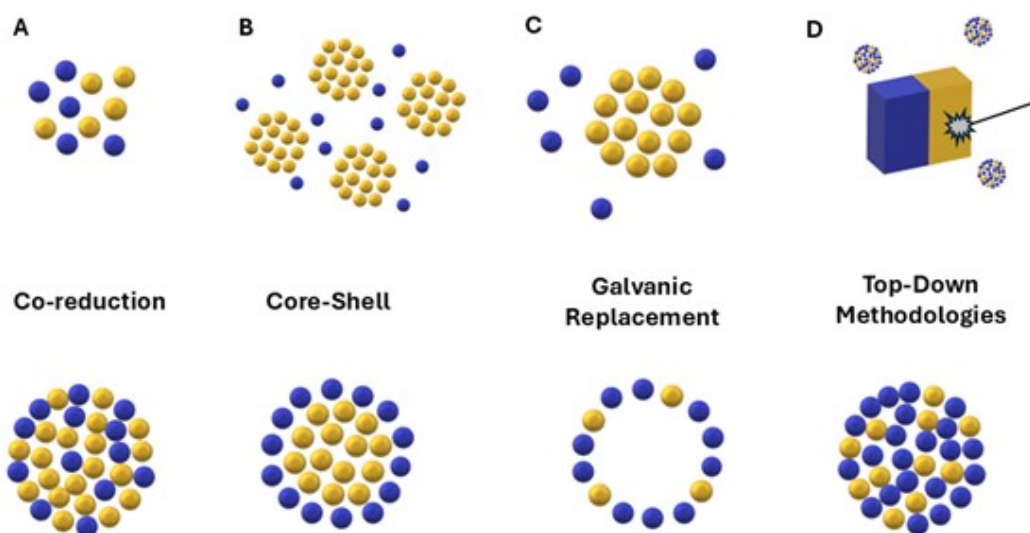


Figure 9. Schematic illustration of common synthetic strategies for bimetallic NPs. (A) Co-reduction: simultaneous reduction of two metal precursors yields alloyed NPs with a mixed atomic distribution. (B) Core-shell growth: sequential nucleation produces NPs where one metal forms the core and the second metal forms the shell. (C) Galvanic replacement: a sacrificial template undergoes partial dissolution, leading to hollow or porous bimetallic structures. (D) Top-down methodologies: bulk alloys are fragmented through processes such as laser ablation, sputtering, or ball milling.

Some of the first reports of these types of materials concerns the growth of Au-labeled SiO₂ particles [77] and a homogeneous SiO₂ shell on Au NPs [78]. These studies were motivated by the necessity of stabilizing the particles without hindering their properties and for this purpose SiO₂ has been proved to be an ideal candidate due to its inertness and transparency. Due to the scarce affinity of Au for SiO₂ (vitreophobic character), caused by the absence of the formation a superficial passivating oxide film in solution and to the presence of organic anions, the NPs had to undergo a functionalization step using aminopropyltrimethoxysilane (APTMS) to prime the surface for the following SiO₂ growth, making it vitreophilic. The SiO₂ growth was then promoted on the NPs acting as nucleation sites, applying the Stöber method via hydrolysis and condensation of tetraethylorthosilicate (TEOS, Si(OC₂H₅)₄) in an alcohol/water mixture [79]. This method had been also applied to the coating of Ag NPs [80] and the first test of this composite system in the catalysis of a redox reaction [81]. Moreover, both Au@SiO₂ and Ag@SiO₂ have been subjected to harsh condition to demonstrate core corrosion. This consequently demonstrates that the SiO₂ layer has an inherently porous character that allows for diffusion of metal ions and/or reagents through the pores [82]. These experiments demonstrated that the SiO₂ layer will not hinder the properties of the metallic core, thus paving the way for a series of applications of these nanocomposites. Further methodologies have been explored to prevent the dissolution of more sensitive cores, such as Ag, and to stabilize NPs before the SiO₂ coating synthesis such as the use of PVP [83], polyethylene glycol (PEG) [84], layer-by-layer (LbL) polyelectrolyte wrapping [85], use of surfactants [86], glucose [87]. To obtain composite nanomaterials with a greater variety of properties and possible applications is it also possible to synthesise a mesoporous silica coating. This type of material is characterized by the presence of ordered pores in between 2 nm and 50 nm in diameter. The first example of a tunable mesoporous silica structure (called MCM-41) (Figure 10) was obtained with the use of surfactants. These surfactants form micelles in the synthesis solution and the micelles form templates that create the mesoporous framework around which the silica precursor will condense to form the final structure. The template was then removed by calcination. For the MCM-41 synthesis the most used surfactant was CTAB [88]. Spherical Au NPs are among the first examples of metallic NPs individually coated with a mesoporous SiO₂ layer [89,90]. In the first reports, the NPs were subjected to the vitreophilization process [78], previously reported for amorphous SiO₂ coatings, and also were coated with a thin layer of dense SiO₂ before the mesoporous coating synthesis. A more direct approach for the mesoporous shell synthesis has been demonstrated on Au nanorods [91], in this process CTAB was used

as both NPs stabilizer and SiO₂ template, without the necessity of the intermediate vitreophilization step. Similarly, the precise control over the shell thickness was achieved by regulating the TEOS amount and addition rates and/or by stopping SiO₂ condensation with PEG-silane at the desired thickness [92]. Since then, different metals and their respective oxides have been encapsulated in a variety of mesoporous SiO₂ shells architectures leading to the application of these composite nanomaterials in a variety of fields (biomedicine, catalysis, sensing, gas storage) [93,94].

2.7. Biogenic synthesis of NPs

Biogenic synthesis of NPs, frequently referred to as "green synthesis," consists of group of methodologies for the synthesis of NPs with the use of naturally sourced molecules and organisms [95,96]. These methodologies can be categorized into two main groups:

- *Plant-mediated*: this group of syntheses includes intracellular and extracellular (plant extracts or extracted phytochemicals) processes. Some plants have the capability of accumulating metals and produce NPs thanks to the variety of molecules present in their structure. While various methodologies exist, the predominant approach involves the utilization of plant extracts. The extracts serve dual roles as reducers and potential stabilizers or capping agents. They are added to the solution containing the metal precursor and, thus, most methodologies are classifiable as "direct syntheses".
- *Microbial synthesis*: several microorganisms such as bacteria, fungi, algae, yeasts and viruses are also reported to synthesize metallic NPs. Depending on the type of microorganism the synthesis can happen intracellularly or extracellularly. The extracellular synthesis method is favoured for its straightforward and simpler purification steps. Conversely, the intracellular synthesis presents challenges and higher costs due to the necessity of additional separation and purification steps. The formation of NPs during the microbial synthesis process occurs through the oxidation/reduction of metallic ions by biomolecules secreted by microbial cells (enzymes, sugars, carbohydrates, proteins). Nonetheless, the microbial synthesis pathways are not yet completely understood due to the variation among the different microorganisms.

Biogenic synthesis of NPs offers clear advantages: it is eco-friendly and produces biocompatible NPs. Some of the synthesised NPs might retain biological activity deriving from the source material and can subsequently be applied in areas such as antimicrobial coatings, agricultural products, and environmental remediation [97,98].

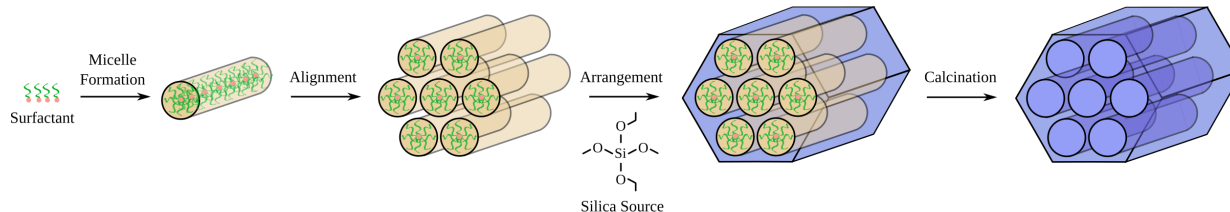


Figure 10. Synthesis pathway of MCM-41. Reproduced from Hermann Luyken - Own work, CC0, [wikimedia.org/w/index.php?curid=32258196](https://commons.wikimedia.org/w/index.php?curid=32258196).

On the other hand, these protocols might also present significant drawbacks. When using plants extracts, the availability of the plants, fruits, and flowers and the composition of their extracts might depend on seasonality, geography and growth conditions, which in turn affects reproducibility, scalability, and NPs purity [97]. The plants or their extract might also have to be preserved before their use, and this increases the energy cost of the process [99]. Similarly, microorganisms might have to be grown for the purpose of synthesis, adding a costly step, in terms of time and energy, to the process. Oftentimes, the NPs obtained with biogenic synthesis lack in monodispersity (size and shape) and stability making their application and scalability more challenging [100,101]. Nevertheless, advances in synthetic protocols continue to improve the morphology and monodispersity of biogenically produced NPs [102].

3. Optical Properties of Metallic NPs

'Metals' optical properties are governed by conduction electrons that move freely on the metal. An electromagnetic source can influence and drive the movement of these electrons. The electromagnetic source can induce an oscillation that resonates with the shape of the metal surface and in this case a surface plasmon resonance is generated [69,103,104].

At the macroscopic level, when an electromagnetic wave interacts with the metal, the electric field of the wave can cause the collective oscillation of the electrons, this phenomenon is known as surface plasmon. The Drude's model describes the frequency at which this collective oscillation occurs as the bulk plasma oscillation frequency (ω_p) (Equation 6).

$$\omega_p = \sqrt{\frac{N_h e^2}{\epsilon_0 m_h}} \quad (6)$$

Where N_h represents the mobile electrons (holes) density, e is the charge of the electron, m_h is the electron (hole) effective mass ϵ_0 is the dielectric permittivity of vacuum.

When metals are in nanometres range, such as in NPs with a size comparable to a wavelength, and all the NPs are illuminated with the appropriate wavelength to produce resonance, then a LSPR is produced. LSPR in NPs depends on several factors, such as the metal type, the size and shape of the NP, and the surrounding media. Every metal has a complex dielectric function (ϵ_m) that depends on the wavelength λ according to the Equation 7:

$$\epsilon_m(\lambda) = \epsilon_{\text{real}}(\lambda) + i\epsilon_{\text{im}}(\lambda) \quad (7)$$

The real part of the dielectric function determines the frequency at which electron oscillation resonance occurs, while the imaginary part incorporates the broadening and absorptive dissipation of this resonance due to damping and dephasing of the electron oscillations. In this context, the dielectric constants for NPs at different wavelengths are assumed to match those of bulk metals. For most metals, excluding some noble and alkali ones, ϵ_{im} is typically very large, which suppresses the excitation of surface plasmons in the visible region. Meanwhile, ϵ_{real} , which correlates with the ability to absorb light, is negative for alkali and noble

metals. In non-noble metals, interband transitions contribute positively to ϵ_{real} , hindering the excitation of surface plasmon modes in small metal spheres. For example, both Au and Ag NPs exhibit intense LSPR, but the Ag LSPR exhibits markedly greater intensity compared to Au. This difference can be attributed to the disparities in their ϵ_{im} . Ag possesses a notably smaller ϵ_{im} , consequently experiencing lower dissipative losses than Au. This translates to a higher scattering quantum yield for Ag NPs, indicating a greater proportion of incident light being scattered as opposed to absorbed.

Furthermore, the narrower bandwidth and sharper LSPR peak observed in Ag NPs can be ascribed to the combination of a smaller ϵ_{im} and a steeper slope (reflecting a greater magnitude) of the real component of the dielectric function ϵ_{real} . This leads to a more restricted range of resonant frequencies, resulting in a sharper peak in the LSPR spectrum. Consequently, Ag NPs surpass Au in terms of their light-scattering efficiency within the vis-NIR region [105]. The size of the NPs affects their optical and electronic properties due to the quantum confinement of the conduction electrons, thus absorption wavelength is directly proportional to the radius of NPs, so as the NP size decreases the LSPR wavelength also decreases (Equation 8):

$$\gamma = \gamma_{\infty} + \frac{A v_f}{R} \quad (8)$$

where γ_{∞} is the scattering rate of the free electrons in bulk metal, A is a constant, v_f is the Fermi velocity of the electrons, and R is the radius of the NPs. The shape of the NPs can change the surface polarization, and therefore LSPR at desired wavelengths can be achieved by synthesising NPs with different morphologies. The relationship between the LSPR shift and shape of particles can be established as in Equation 9:

$$\Delta\lambda = \frac{\Delta N}{2N} \lambda_{\text{sp}} \sqrt{\epsilon_{\infty} + \left(\frac{1-\eta}{\eta}\right) \epsilon_{\text{medium}}} \quad (9)$$

Where N is the electron density in the metals, λ_{sp} is the SPR wavelength for metals, ϵ_{∞} is the high-frequency contribution to the metal dielectric function, ϵ_{medium} is the dielectric constant of the medium, and η is the particle shape factor.

In addition to the dipolar mode (**Figure 11**), which is the most commonly observed and studied mode, higher-order modes such as the quadrupole and octupole LSPR can also occur in plasmonic NPs. These higher-order modes involve more complex charge distributions within the NP, resulting in resonances at higher energies compared to the dipolar mode. The quadrupole LSPR involves the collective oscillation of electrons along two perpendicular axes, leading to a quadrupolar charge distribution within the nanoparticle. Similarly, the octupole LSPR involves the collective oscillation of electrons along three perpendicular axes, resulting in an octupolar charge distribution. Because of the more complex charge distributions involved in higher-order modes, their energies typically increase with increasing multipole order. This means that quadrupole LSPR occurs at higher energies than dipole LSPR, and octupole LSPR occurs at even higher energies than quadrupole LSPR (**Figure 12**) [106]. Moreover, LSPR is sensitive to the surrounding medium and its absorption wavelength maximum

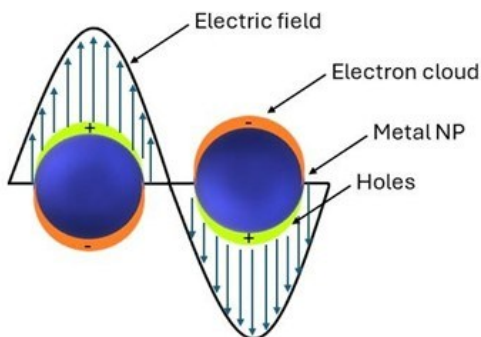


Figure 11. Illustration of the dipolar surface plasmon resonance, with the collective oscillation of the conduction band electrons due to an incident electric field.

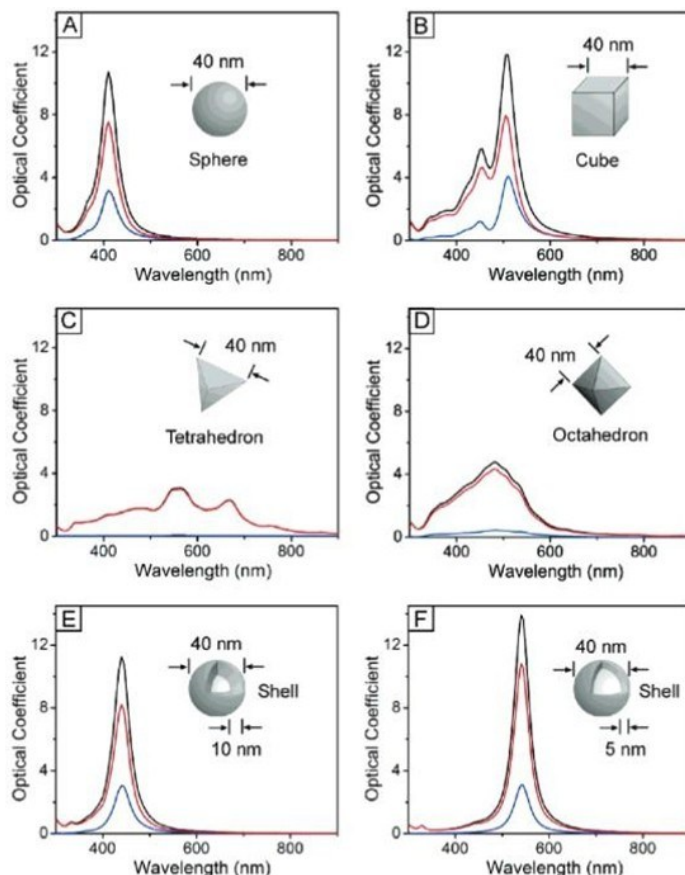


Figure 12. Calculated UV-vis extinction (black), absorption (red), and scattering (blue) spectra of Ag nanostructures, illustrating the effect of a nanostructure's shape on its spectral characteristics. An isotropic sphere (A) exhibit spectra with a single resonance peak. Anisotropic cubes (B), tetrahedra (C), and octahedra (D) exhibit spectra with multiple, red-shifted resonance peaks. The resonance frequency of a sphere red-shifts if it is made hollow (E), with further red-shift for thinner shell walls (F). Reproduced with permission from reference [106] Copyright 2006 American Chemical Society.

λ_{max} changes as the dielectric constant ϵ or refractive index n of the medium is changed. The LSPR frequency can then also be shifted by varying the environment (stabilizer, functionalization or solvent molecules) and as a consequence the dielectric constant of the NPs-environment system. The field induced by the conjunct of NPs and their medium can be written in the form of effective polarizability and dipole moment as given by Equation 10:

$$\rho = \epsilon_m \alpha E_0 \quad (10)$$

Where ρ is the effective dipole moment of the NP-medium system, E_0 is the incident electric field, α is the dipolar polarizability and ϵ_m is the dielectric constant of embedding media. When the NPs are coated with a dielectric material of thickness d and dielectric constant ϵ_d , then polarizability α is defined by Equation 11:

$$\alpha = 4\pi\epsilon_0(R+d)^3 \frac{\epsilon_d\epsilon_a - \epsilon_a\epsilon_b}{\epsilon_d\epsilon_a + 2\epsilon_m\epsilon_b} \quad (11)$$

Where a is the NP's radius and ϵ_a is the dielectric constant of the NP. Similarly, b is the total radius of the NP-medium system and ϵ_b is the dielectric constant of the NP-medium system. A red-shift in

absorption spectra is observed with the increase in the dielectric constant of the environment. The magnitude of the spectral shift $\Delta\lambda$ for NPs is described in Equation 12:

$$\Delta\lambda_{\max} = m\Delta n \left(1 - e^{-\frac{2d}{\ell d}} \right) \quad (12)$$

Where m is the bulk refractive-index response of the NPs, Δn is the change in the refractive index induced by the adsorbate, d is the effective adsorbate layer thickness, and ℓd is the characteristic electromagnetic field decay length. Thus, shell materials with a higher refractive index will lead to a larger red-shift with broadening of LSPR peaks.

4. Application of Metallic NPs

Metallic NPs, thanks to the huge variety of structures and composition, play a crucial role in various fields, from electronics to healthcare to agriculture and environmental remediation [93,107]. Some of these applications, where plasmonic and composite NPs are applied, are discussed below.

4.1. Healthcare

The healthcare sector includes a diverse array of needs and applications. A few applications where NPs have an impact are presented below.

4.1.1. Antibacterial activity and Antibiotic resistance

In recent years, significant efforts have been directed towards addressing the ever increasing problem of antibiotic resistance [108], whether by seeking alternatives or enhancing the efficacy of existing antibiotics through the integration of nanomaterials. Additionally, great efforts have been devoted to exploring methods to prevent bacterial proliferation on surfaces and biofilm formation. Ag NPs are undoubtedly the most extensively studied NPs for mitigating antibiotic resistance as their antibacterial properties have been known for centuries [109]. However, more recently also Cu and ZnO NPs have been investigated for their intrinsic antibacterial activity [110,111]. Ag and ZnO NPs have demonstrated synergistic effect with several antibiotics against a variety of bacteria through diverse modes of action, such as metal ions release, non-oxidative and oxidative stress [112–114]. Additionally, Ag, Cu, and ZnO NPs have shown the ability to synergize with conventional antibiotics and disrupt bacterial efflux pumps, a key mechanism involved in biofilm formation [115]. Research has concluded that Ag NPs can enhance the efficacy of antibiotics against pathogens commonly encountered in veterinary medicine, regardless of antibiotic resistance [116]. NPs with antibacterial properties can be also integrated in devices. Ag, Au, Cu, ZnO and TiO₂ have demonstrated to be able to increase the antibacterial properties of chitosan when applied as wound dressing to avoid bacterial contamination and infections, and also by enhancing healing through the regulation of re-epithelialisation and inflammation [117]. Moreover, medical implants, catheters, and healthcare fabrics can be integrated with metallic antibacterial NPs to mitigate infection risks and bacterial transmission in

healthcare setting [118]. Tri-elemental AgCuMg NPs, despite being in the early stages of development, have demonstrated antibacterial activity against both gram-positive and gram negative bacteria when integrated into coatings [119]. Similarly, hydrogel coatings loaded with Cu NPs have exhibited pronounced antibacterial properties and adhered well to stainless steel medical equipment [120]. Recent research has emphasised the significance of surface topographies in conferring antibacterial properties. Different morphologies found in nature are being studied for their potential to further enhance antibacterial surfaces. The combination of antibacterial surface topographies and antibacterial NPs holds promise in reducing infections and controlling their spread [121,122]. The primary drawbacks of using NPs for their antibacterial properties might be a limited stability on the NPs and an excessively fast ions release from the particle. Composite NPs, such as Ag@mesoporous SiO₂ NPs, have the potential to overcome these disadvantages and confer superior properties compared to bare NPs. Thanks to the accessible and porous network of the protective SiO₂ layer, the encapsulated nanocrystals can release antibacterial Ag ions in a steadier and continuous manner [123], furthermore the SiO₂ shell can help to prevent aggregation and increase the NPs solubility. The mesoporous channels can then be additionally used for encapsulation of active molecules, such as antibiotics, to treat antibiotic resistant infections [124] or to accelerate the healing of infected wounds [125].

4.1.2. Imaging, diagnosis and cancer treatment

Plasmonic NPs, due to their unique optical properties, find applications in diagnostics, particularly for biomedical imaging of tissues and for the detection of cancer cells. The composition and the shape of the NPs are adjustable, thus making it possible to tune the NPs based on the desired scattering [126]. For instance, NPs that scatter light in the near-infrared (NIR) range allow for a high-resolution deep tissue bioimaging [127]. Furthermore, NPs can be functionalized with antibodies, aptamers, or peptides to confer specific cellular binding features, thereby enhancing imaging precision and detection sensitivity. The functionalized NPs can be assembled to obtain a "detection kit" for a series of different diseases [128,129]. Coating NPs with a mesoporous SiO₂ shell can increase the biocompatibility and the cell up-take of the nanomaterial making them suitable for potential in vivo imaging applications. For example, biomolecule - conjugated Au nanorods encapsulated in a mesoporous SiO₂ shell were specifically taken up by cancer cells *in vitro* [130]. Mesoporous SiO₂ can also be modified with functional groups and conjugated with biomolecules for specific labelling of cells. Photoacoustic imaging, an emerging technique in biomedical imaging, can be significantly enhanced through the use of plasmonic NPs as contrast agents. In this imaging modality, a short laser pulse is directed onto the tissue under examination, causing rapid thermal expansion and the generation of ultrasound waves. These waves are then captured by ultrasound transducers and translated into high-resolution images. Au NPs are favoured in this application due to their biocompatibility, ease of functionalization, and adjustable LSPR. Current research efforts are concentrated on optimizing NPs for photoacoustic imaging within the second NIR window (1000 - 1700 nm). This spectral range

offers reduced background noise and scattering in biological tissues, thereby facilitating clearer and more precise imaging [131]. Other than diagnosis, plasmonic NPs can also find application in therapy. When plasmonic NPs are irradiated at their resonance wavelength they will generate a temperature rise in their proximity. This effect has found application in photothermal therapy, that is a non invasive technique utilized for cancer treatment. Plasmonic NPs, and particularly Au NPs are excellent candidates for this therapy due to the easy cell take-up, easy functionalization for specific cells targeting, and easy LSPR tuning. For photothermal therapy, the 650 - 900 nm range is preferred for application because minimal skin and tissue absorption allows light to penetrate deep into tissues in a non-invasive manner. The generated heat can induce thermal damage to cancer cells, leading to their destruction and vascular disruption that consist in damaging the tumour's blood vessels, compromising the tumour's viability [132,133]. Composite NPs can also add extra functionalities to the phototherapeutic treatment such as the delivery of a drug encapsulated in a mesoporous structure [134,135] or in a hollow plasmonic structure [136]. The generated heat can act as a trigger for the release of an encapsulated drug, while profiting of the augmented cell membrane permeability due to higher temperature [93,137]. Additional functionalities, such as magnetic properties, can enhance the NPs targeting of cancer cells through magnetic-guided photothermal therapy [138].

4.2. Sensing

4.2.1. Plasmonic sensing

NPs are particularly sensitive to their surrounding environment and this property made them to find application as plasmonic sensors for ex-situ analysis. Plasmonic sensors can detect subtle changes reflected in modifications of the LSPR of the colloidal system. Due to their outstanding optical properties, Au and Ag NPs are mostly used for this type of sensing. Analytes can be detected in a *yes/no* fashion or also quantified as a consequence of different phenomena [139]:

- *Analyte detection based on aggregation of NPs:* the addition of analytes to the colloidal system can cause a decrease the inter-particle distance of the NPs leading to their aggregation and to a change in shape and position of the LSPR. The amount of analyte can be estimated with spectroscopic or colorimetric techniques [140,141].
- *Analyte detection based on oxidation of NPs:* in the presence of analyte NPs can undergo oxidation, thus the number of metallic NPs in solution will decrease leading to a change in the colour of the solution and of the LSPR intensity. The analyte quantity can then be estimated observing the changes at a specific wavelength [142].
- *Analyte detection based on dimensional change of NPs:* certain analytes can cause a change the morphology/dimension of the NPs. In this case, a change in the LSPR profile will be observed, some bands will be quenched while others might appear [143].

Plasmonic NPs applied in sensing might undergo extra functionalization with different molecules such as oligonucleotides, proteins and amino acids, organic polymers, and organic

compounds. Functionalized plasmonic NPs can provide specificity towards target analytes, allowing for higher selectivity and sensitivity in the detection process. Functionalization can enhance the stability and dispersibility of the NPs and further regulate the detection mechanisms [144].

4.2.2. Surface-Enhanced Raman Spectroscopy

Raman scattering is inherently a weak phenomenon up to ten orders of magnitude weaker than fluorescence [145], but it offers high specificity. The combination of Raman's specificity with the plasmonic field enhancement provided by plasmonic nanostructures, known as Surface-Enhanced Raman Spectroscopy (SERS), first observed in 1973 for pyridine adsorbed on a roughened silver electrode [146], can exponentially increase the intensity of Raman signals, enabling the detection of even single molecules of analyte [107,147,148]. Molecules adsorb onto the surface of metallic nanostructures, and when laser light is directed onto the substrates, it interacts with the LSPR of the NPs, resulting in a significant enhancement of the Raman scattering signal. SERS can be performed either in a colloidal solution or, more commonly, with the solution containing the analyte deposited on a surface previously functionalized with metallic NPs. The shape, size, and arrangement of the NPs greatly influence the enhancement of the Raman signal. Au and Ag NPs, both in pure and alloyed compositions, are the most commonly used. A greater field enhancement occurs when NPs exhibit tips, cavities, and overall anisotropic morphology [145]. Additionally, the disposition and inter-particle distances of the NPs determine the effectiveness of a SERS substrate [147], in this case SiO₂ shells can be employed to further regulate the arrangement and distances between NPs. Mesoporous SiO₂ is generally preferred, as its channels permit the diffusion of analyte molecules to come into proximity with the metallic surface. Moreover, the shell can serve a protective function, increasing the stability of the NPs and preventing possible aggregations and reshaping phenomena [93].

4.2.3. Surface-Enhanced Fluorescence

The phenomenon of fluorescence is widely used in sensing, thanks to its fastness, reliability and high sensitivity. However, the major limitation is constituted by the quantum yield and fluorescence lifetime of the fluorophore [149]. Similarly to SERS, plasmonic near-field enhancement can enhance the light emission by fluorophores located in close vicinity of metallic nanostructures, in a phenomenon known as Surface-Enhanced Fluorescence (SEF). A crucial parameter for SEF is the distance between the NPs and the analyte molecules. Fluorophores can not, in fact, be in contact with the metallic surface, otherwise their emission will be quenched, while a distance of a few nm will dramatically increase it. As spacers, either thin metal oxide layer or SiO₂ layers can be used, the latter being more flexible regarding the possibility of synthesising shells with different thicknesses. SiO₂ shells can be also further functionalized to increase the detection of specific analytes [93]. Alloyed NPs with tunable composition and SiO₂ shells with multiple functionalisation's, combining the scattering of NPs and the SEF effect, can provide a platform for multiplex-detection allowing for the detection of numerous targets within the same

sample, thus providing a comprehensive view of the system [107,150].

4.3. Catalysis

Catalytic processes have brought significant advancements in research and technology, enabling the production of fertilizers, plastics, chemicals, and environmental remediation, such as the catalytic removal of pollutants from car exhausts.

4.3.1. Metallic NPs in catalysis

Metallic NPs have shown potential in the field of catalysis, as their properties are different from the one of their bulk counterparts and the reduction of the size brings an increment in the high surface to volume ratio, and thus active sites for the catalysis to happen. The composition, size and shape of the NPs are of great importance in the determination of the catalytic properties of the nanocrystals. For example, Au bulk surfaces are known to be inert, but in 1987 it was discovered that Au NPs were effective for low temperature CO oxidation [151,152]. Decreasing the size of the NPs can lead to an increase in the number of corner atoms and edges, that will lead to a higher degree of surface unsaturation. This variation can impact the bond strength of reaction intermediates with the catalyst, while corners and edges also offer diverse surface configurations for molecules to adsorb [153–155]. An increase in edges and corners is also obtainable with the synthesis of anisotropic NPs. Shape, that means which crystal facets are exposed to the reagents, has a significant importance on the catalytic properties of the NPs. Specifically, NPs that present tips and edges, considered active sites for the catalytic reaction, usually display better properties. When NPs have a quasi-spherical shape and exhibit only (111) low energy facets, their catalytic efficiency is usually lower compared to NPs of the same metal but with different morphologies that expose higher

energy (100) facets [156]. Furthermore, shape can also determine the selectivity of a reaction, for example in the benzene hydrogenation over cubic and cuboctahedral Pt NPs. Cuboctahedral NPs, characterized by the presence of (111) facets, lead to the formation of cyclohexane and cyclohexene, while cubic NPs, characterized by the presence of (100) facets, only lead to the formation of cyclohexane [152,157].

4.3.2. Composite NPs in catalysis

Composite NPs can have a prominent role in catalysis thanks to the great variety of combinations of structures and materials. Metallic NPs, for instance, can be encapsulated within various materials and with different architectures such as core@shell and yolk@shell configurations, and supported by diverse substrates including MOFs, carbon, and dendrimers (**Figure 13**) [158]. The encapsulation of single catalytic NPs in a core@shell structure can offer several advantages, such as adding extra stabilization and protection and prolonging the life of the catalyser. Multicore core@shell NPs or non coated NPs can in fact face aggregation of the cores both in colloidal solution or during high temperature catalytic processes. An aggregation will inevitably bring to a loss of catalytic sites and consequently a decrease in the catalytic efficiency [159]. The yolk@shell architecture, often referred to as nanoreactor in the catalysis field, offers additional advantages compared to the core@shell structure. As the core is able to freely move inside the protective shell, there is more surface area, and thus more catalytic sites available [160]. Encapsulated structures can furthermore manifest a greater selectivity. The pores' size, either in nanoreactors or supports architectures [161], can be finely tuned to act as a molecular sieve and regulate molecular diffusion [158]. Extra functionalities can also be added to the surface of metallic NPs to improve the catalytic reaction rates [162].

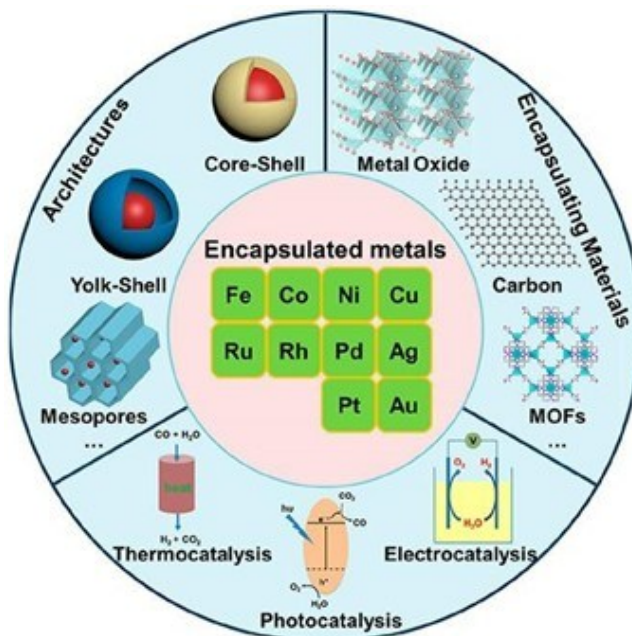


Figure 13. Encapsulated metal NPs with different architectures for catalytic applications. Reproduced with permission from reference [158] Copyright 2020 American Chemical Society.

Composite bimetallic NPs have emerged as a promising class of catalysts, offering unique properties and enhanced catalytic performance compared to their monometallic counterparts. By combining two different metals within the same NP, bimetallic NPs can exhibit synergistic effects, where the properties of the individual metals are combined and amplified, leading to improved catalytic activity and selectivity [163]. Bimetallic NPs can exhibit features on their surface such as migration, segregation, isolation of single atoms, surface enrichment, leading to the formation of structures with enhanced catalytic activity [164]. Pd based PdZn and PdPt bimetallic NPs, due to an increase of defects in the NPs structure and a change the electronic properties of the catalyst (ligand effect), demonstrated superior properties when compared to the Pd monometallic counterpart in the selective hydrogenation of dehydrolinalool [165]. PtAu NPs showed excellent properties in the reduction of 4-nitrophenol. The authors believe that the alloying of Pt and Au induces a strong synergistic effect that increase the catalytic activity, compared to pure Pt and pure Au NPs, by altering the electronic structure and the preferential adsorption of oxygen [166]. Ni@Pt NPs exhibited more than twice the catalytic activity of Pt NPs synthesized using the same method. ORR experiments demonstrated a significant enhancement in the activity of Ni@Pt catalysts compared to Pt alone. This increase in catalytic activity is attributed to alterations in geometric and/or electronic properties, which can influence the binding energy of oxygen and the adsorption of bisulfate anions [167].

4.3.3. Photocatalytic applications

Plasmonic metal NPs, either monometallic or bimetallic, due to their peculiar optical properties can be successfully employed in photocatalytic processes. The photocatalysts employed for a diverse range of chemical reactions under UV-visible light, are predominantly semiconductors. In such systems, semiconductors absorb photons, generating high-energy charge carriers (electron-hole pairs) within the semiconductor material. These charge carriers then dissociate and migrate to catalytically active sites situated at the semiconductor/liquid interface, where they facilitate various chemical transformations [168]. The most frequently utilized semiconductor is TiO₂. Because of its large band gap (3.0 - 3.2 eV), TiO₂ primarily absorbs light in the near UV region (<400 nm), which constitutes only a small portion of solar radiation (approximately 5%) [169]. Plasmonic NPs and semiconductors have emerged as a feasible combination to harvest a higher range of the solar spectrum. When deposited on TiO₂, a Schottky barrier will form at the interface between NPs and TiO₂, thus facilitating the electron-hole pairs separation and consequently enhancing the lacking photocatalytic activity of semiconductor materials under visible light [170].

AgAu NPs on TiO₂ have been used to degrade phenol in aqueous solution under visible light with more efficiency than Au NPs on TiO₂ [171]. The authors propose that the enhanced activity is attributed to electron transfer mechanisms. The presence of bimetallic NPs impedes charge recombination on Au NPs by facilitating electron transfer to Ag, known for its electron accepting abilities, and subsequently to the TiO₂ conduction band, facilitating the oxidation of phenol molecules by O₂ to form benzoquinone on

the AgAu surface, while keeping it in a reduced state. AuPd NPs on TiO₂ were used to demonstrate that the relative composition and the structure of the bimetallic NPs have influence on the photochemical H₂ evolution from ethanol aqueous solution. Core@shell Au@Pd bimetallic NPs showed the highest activity and NPs with a higher Pd content showed enhanced photoactivity, attributed to the fact that a thicker Pd shell supposedly shields photogenerated electrons from the recombination with holes [172]. Monometallic NPs deposited on TiO₂ were also utilized in water splitting and H₂ generation. Au NPs have successfully produced H₂ generation under visible light illumination, several experiments demonstrated the importance of different parameter such as the phase of the TiO₂ [173], and the size of the Au NPs [174]. Other than Au NPs, also monometallic Ag NPs [175] and Cu NPs [176] have been used for the same catalytic reaction. Cu NPs constitute a valid alternative to the rarer and more valuable Au and Ag.

Photocatalysis mediated by plasmonic NPs has proven an excellent tool in the field of environmental remediation. Several studies highlighted the potential degradation of pollutants either by NPs in solution or supported on TiO₂. Molecules such as methylene blue, rhodamine B, phenol are often chose as model for pollutants. Bio-synthesised CuO NPs [177], Ag NPs [178], degraded methylene blue and crystal violet in solution under sunlight. Supported NPs offer easier handling, recovery and the combination effect of the semiconductor support. Ag and Au NPs on mesoporous TiO₂ were tested for the degradation, as water pollutant models, of the azo dyes (congo red, methyl orange, acid orange 10, and remazol red) under solar and visible light irradiations. Both NPs improved the performance of TiO₂ with the Au NPs appearing to be the most promising candidates [179]. Photocatalysis can also be applied in the degradation of a class of rapidly emerging indoor pollutants known as volatile organic compounds (VOCs), of which examples are formaldehyde, acetaldehyde, methanol, ethylene, toluene.

Au supported on TiO₂ can degrade formaldehyde in air and under visible light. For the oxidation to happen the moisture present in the air has a decisive effect and visible light seems to accelerate the rate-determining steps of the reaction, leading to an overall possible degradation process for this VOC in ambient conditions [180]. Au@TiO₂ core@shell and yolk@shell structures demonstrated photocatalytic activity for the oxidation of gaseous toluene under visible light illumination. The yolk@shell architecture, with greater surface area and numerous mesoporous channels that can enhance the absorption of VOCs and provide more active sites, proved to have the best activity and reusability [181]. Photocatalysis offers a potential solution to the energy crisis and rising CO₂ emissions caused by human activities. CO₂ is a highly stable molecule and conventional thermolysis methods used for CO₂ degradation require harsh conditions and thus high energy consumption [169]. CO₂ photocatalytic conversion aided by plasmonic NPs is a hugely studied process and promising result have already been reported in the obtention of valuable products such as CH₄, CH₃OH, and C₂H₅OH. NPs of different compositions supported on different TiO₂ structures have been tested for CO₂ reduction. Au NPs and Pt NPs on TiO₂ nanofibers surpassed the catalytic properties of the semiconductor alone thanks to the synergistic effect of the two types of metals, Au LSPR effect that improves charge separation in

the semiconductor and Pt NPs which serve as electron-sink and active site. Ag NPs loaded on TiO₂ nanotube arrays promote a more efficient CO₂ reduction thanks to the LSPRs properties of Ag. When exposed to light hot electrons will be generated on the Ag NPs which are subsequently injected into the conduction band of TiO₂, promoting efficient charge separation and hindering electron-hole recombination. Furthermore, the localized near-field effect induced by the Ag NPs accelerates the transport of electrons within the nanotubes, leading to improved charge carrier transport efficiency [182]. Highly crystalline Cu NPs deposited onto anatase TiO₂ were found to convert CO₂ into CO while suppressing the competitive mechanism of hydrogen evolution. This study also highlighted the importance of the careful consideration of the most beneficial amount of NPs, as an excessive quantity of Cu demonstrated to be undesirable for the reaction [183].

4.4. Energy

The transition from fossil to alternative fuels is crucial for a sustainable and healthy future for our planet. Plasmonic NPs have gained attention as a possible solution to increase the exploitation of solar energy [184]. Plasmonic NPs, thanks to their absorption and scattering properties, can be efficiently integrated in solar light harvesting devices to maximize their harvesting capability [93].

Au NPs, with a size of approximately 45 nm, were incorporated into organic photovoltaic solar cells (OPVs) based on polymers. The resulting plasmonic enhanced OPV device exhibited a significant increase in light absorption due to localized field enhancement induced by LSPR, without compromising the device's electrical properties [185]. A further improvement in VOCs performance can be promoted by utilizing NPs protected by a SiO₂ shell. Core@shell particles can, in fact, be partially embedded on the active layer interface of the device. The SiO₂ shell serves many purposes such as maintaining the desired inter-particle distance and preventing changes in the morphology of the particle [186]. Similarly, NPs can be incorporated in dye-sensitized solar cells (DSSC). These cells utilize the light-absorbing properties of dyes, particularly in the visible range, to sensitize a metal oxide film, usually TiO₂. To take advantage of the absorption properties of plasmonic NPs, the use of anisotropic NPs and mixtures of different morphologies has been explored. For example, studies have shown that Au@Ag₂S nanorods [187] and mixtures of Ag NPs [188] can enhance the efficiency of DSSC devices due to their broader light absorption range compared to the commonly used spherical NPs.

5. Conclusions

Metallic NPs provide an exceptional platform for exploring the relationship between synthesis, structure, and functionality. As discussed throughout this review, the choice of synthetic strategy, whether top-down, bottom-up, direct, or seed-mediated, determines the resulting morphology, stability, and performance of the material. A solid understanding of the principles governing nucleation, growth, and stabilization is therefore essential to design NPs with properties tailored to specific functions. Beyond their

synthesis, the optical, catalytic, and biological behaviours of metallic NPs illustrate how nanoscale features influence macroscopic performance. Their LSPRs enable powerful sensing techniques, while catalytic activity can be precisely adjusted through control of size, shape, and composition. Applications across healthcare, energy, and environmental monitoring demonstrate both their versatility and growing relevance.

By combining historical developments, theoretical insights, and practical considerations, this introductory review seeks to clarify the connections between synthetic methods and resulting properties. The intention is not only to describe the main strategies available but also to encourage critical analysis, creative experimental design, and continued exploration of improved synthetic approaches.

Acknowledgements

S.N. thanks the FCT/MCTEC (Fundação para a Ciência e Tecnologia and Ministério da Ciência, Tecnologia e Ensino Superior) Portugal for her doctoral grant associated with the Chemistry PhD program (SFRH/BD/144618/2019). This work was supported by the Associate Laboratory for Green Chemistry LAQV which is financed by national funds from Fundação para a Ciência e Tecnologia and Ministério da Ciência, Tecnologia e Ensino Superior (FCT/MCTES) through the the project UID/50006/2023 of the Associate Laboratory for Green Chemistry - LAQV REQUIMTE, details here: <https://laqv.requimte.pt/a/74-funding>. PROTEOMASS Scientific Society (Portugal) is also acknowledged by the funding provided through the General Funding Grants 2024-2025.

References

- [1] J. Ogden, *Interdiscip. Sci. Rev.* 17 (1992) 261–270. DOI: 10.1179/030801892791925475
- [2] S. Medici, M. Peana, V.M. Nurchi, M.A. Zoroddu, *J. Med. Chem.* 62 (2019) 5923–5943. DOI: 10.1021/acs.jmedchem.8b01439
- [3] D.A. Scott, W. Bray, *Platin. Met. Rev.* 24 (1980) 147–157. DOI: 10.1595/003214080X244147157
- [4] M. Radetzki, *Resour. Policy* 34 (2009) 176–184. DOI: 10.1016/j.resourpol.2009.03.003
- [5] J. Pérez-Arantegui, J. Molera, A. Larrea, T. Pradell, M. Vendrell-Saz, I. Borgia, B.G. Brunetti, F. Cariatì, P. Fermo, M. Mellini, A. Sgamellotti, C. Viti, *J. Am. Ceram. Soc.* 84 (2001) 442–46. DOI: 10.1111/j.1151-2916.2001.tb00674.x
- [6] F. Antonii, *Panacea Aurea, Sive Tractatus Duo de Ipsius Auro Potabili, Ex Bibliopolio Frobeniano*, Hamburg, 1618.
- [7] J. Kunckel, *Nuetliche Observationes Oder Anmerkungen von Auro Und Argento Potabili*, Hamburg, 1676.

- [8] C. Chan, (2008). DOI: <https://www.sciencehistory.org/stories/magazine/from-nanotech-to-nanoscience/>
- [9] The Stained Glass Association of America, (2025). DOI: <https://stainedglass.org/learning-resources/history-stained-glass>
- [10] I. Freestone, N. Meeks, M. Sax, C. Higgitt, *Gold Bull.* 40 (2007) 270–277. DOI: 10.1007/BF03215599
- [11] R. November, R. February, *Philos. Trans. R. Soc. London* 147 (1857) 145–181. DOI: 10.1098/rstl.1857.0011
- [12] D. Thompson, *Gold Bull.* 40 (2007) 267–269. DOI: 10.1007/BF03215598
- [13] J. Turkevich, P.C. Stevenson, J. Hillier, *Discuss. Faraday Soc.* 11 (1951) 55. DOI: 10.1039/df9511100055
- [14] G. Mie, *Ann. Phys.* 330 (1908) 377–445. DOI: 10.1002/andp.19083300302
- [15] N. Abid, A.M. Khan, S. Shujait, K. Chaudhary, M. Ikram, M. Imran, J. Haider, M. Khan, Q. Khan, M. Maqbool, *Adv. Colloid Interface Sci.* 300 (2022) 102597. DOI: 10.1016/j.cis.2021.102597
- [16] P.G. Jamkhande, N.W. Ghule, A.H. Bamer, M.G. Kalaskar, *J. Drug Deliv. Sci. Technol.* 53 (2019) 101174. DOI: 10.1016/j.jddst.2019.101174
- [17] J. Polte, *CrystEngComm* 17 (2015) 6809–6830. DOI: 10.1039/C5CE01014D
- [18] N.T.K. Thanh, N. Maclean, S. Mahiddine, *Chem. Rev.* 114 (2014) 7610–7630. DOI: 10.1021/cr400544s
- [19] R. Becker, W. Döring, *Ann. Phys.* 416 (1935) 719–752. DOI: 10.1002/andp.19354160806
- [20] V.K. LaMer, R.H. Dinegar, *J. Am. Chem. Soc.* 72 (1950) 4847–4854. DOI: 10.1021/ja01167a001
- [21] W. Ostwald, *Zeitschrift Für Phys. Chemie* 34U (1900) 495–503. DOI: 10.1515/zpch-1900-3431
- [22] J.R. Shimpi, D.S. Sidhaye, B.L. V Prasad, *Langmuir* 33 (2017) 9491–9507. DOI: 10.1021/acs.langmuir.7b00193
- [23] M. José-Yacamán, C. Gutierrez-Wing, M. Miki, D.-Q. Yang, K.N. Piyakis, E. Sacher, *J. Phys. Chem. B* 109 (2005) 9703–9711. DOI: 10.1021/jp0509459
- [24] E.J.H. Lee, C. Ribeiro, E. Longo, E.R. Leite, *J. Phys. Chem. B* 109 (2005) 20842–20846. DOI: 10.1021/jp0532115
- [25] T.L. Moore, L. Rodriguez-Lorenzo, V. Hirsch, S. Balog, D. Urban, C. Jud, B. Rothen-Rutishauser, M. Lattuada, A. Petri-Fink, *Chem. Soc. Rev.* 44 (2015) 6287–6305. DOI: 10.1039/C4CS00487F
- [26] N. Shirtcliffe, U. Nickel, S. Schneider, *J. Colloid Interface Sci.* 211 (1999) 122–129. DOI: 10.1006/jcis.1998.5980
- [27] N.G. Bastús, F. Merkoçi, J. Piella, V. Puentes, *Chem. Mater.* 26 (2014) 2836–2846. DOI: 10.1021/cm500316k
- [28] Y. Ishida, T. Jirasupangkul, T. Yonezawa, *New J. Chem.* 39 (2015) 4214–4217. DOI: 10.1039/C5NJ00420A
- [29] N.R. Jana, L. Gearheart, C.J. Murphy, *J. Phys. Chem. B* 105 (2001) 4065–4067. DOI: 10.1021/jp0107964
- [30] Y. Sun, B. Gates, B. Mayers, Y. Xia, *Nano Lett.* 2 (2002) 165–168. DOI: 10.1021/nl010093y
- [31] N.G. Bastús, J. Comenge, V. Puentes, *Langmuir* 27 (2011) 11098–11105. DOI: 10.1021/la201938u
- [32] Y. Xia, K.D. Gilroy, H. Peng, X. Xia, *Angew. Chemie Int. Ed.* 56 (2017) 60–95. DOI: 10.1002/anie.201604731
- [33] L. Scarabelli, M. Sun, X. Zhuo, S. Yoo, J.E. Millstone, M.R. Jones, L.M. Liz-Marzán, *Chem. Rev.* 123 (2023) 3493–3542. DOI: 10.1021/acs.chemrev.3c00033
- [34] T.-H. Yang, J. Ahn, S. Shi, P. Wang, R. Gao, D. Qin, *Chem. Rev.* 121 (2021) 796–833. DOI: 10.1021/acs.chemrev.0c00940
- [35] A. Guerrero-Martínez, S. Barbosa, I. Pastoriza-Santos, L.M. Liz-Marzán, *Curr. Opin. Colloid Interface Sci.* 16 (2011) 118–127. DOI: 10.1016/j.cocis.2010.12.007
- [36] R. Jin, Y. Cao, C.A. Mirkin, K.L. Kelly, G.C. Schatz, J.G. Zheng, *Science* (80-.). 294 (2001) 1901–1903. DOI: 10.1126/science.1066541
- [37] S. Chen, D.L. Carroll, *Nano Lett.* 2 (2002) 1003–1007. DOI: 10.1021/nl025674h
- [38] Q. Zhang, Y. Hu, S. Guo, J. Goebel, Y. Yin, *Nano Lett.* 10 (2010) 5037–5042. DOI: 10.1021/nl1032233
- [39] C.H. Zhang, J. Zhu, J.J. Li, J.W. Zhao, *ACS Appl. Mater. Interfaces* 9 (2017) 17387–17398. DOI: 10.1021/acsami.7b04365
- [40] Y. Huang, A.R. Ferhan, Y. Gao, A. Dandapat, D.H. Kim, *Nanoscale* 6 (2014) 6496–6500. DOI: 10.1039/c4nr00834k
- [41] Y. Sun, B.T. Mayers, Y. Xia, *Nano Lett.* 2 (2002) 481–485. DOI: 10.1021/nl025531v
- [42] M.A. Mahmoud, M.A. El-Sayed, *Langmuir* 28 (2012) 4051–4059. DOI: 10.1021/la203982h

- [43] Z. Leng, X. Wu, X. Li, J. Li, N. Qian, L. Ji, D. Yang, H. Zhang, *Nanoscale Adv.* 4 (2022) 1158–1163. DOI: 10.1039/D1NA00842K
- [44] L. Lu, A. Kobayashi, K. Tawa, Y. Ozaki, *Chem. Mater.* 18 (2006) 4894–4901. DOI: 10.1021/cm0615875
- [45] Y.-H. Chen, H.-H. Hung, M.H. Huang, *J. Am. Chem. Soc.* 131 (2009) 9114–9121. DOI: 10.1021/ja903305d
- [46] Mahmoud, C.E. Tabor, M.A. El-Sayed, Y. Ding, Z.L. Wang, *J. Am. Chem. Soc.* 130 (2008) 4590–4591. DOI: 10.1021/ja710646t
- [47] Z. Fang, Y. Zhang, F. Du, X. Zhong, *Nano Res.* 1 (2008) 249–257. DOI: 10.1007/s12274-008-8029-0
- [48] J.D. Hoefelmeyer, K. Niesz, G.A. Somorjai, T.D. Tilley, *Nano Lett.* 5 (2005) 435–438. DOI: 10.1021/nl048100g
- [49] N.M. Ngo, H.-V. Tran, T.R. Lee, *ACS Appl. Nano Mater.* 5 (2022) 14051–14091. DOI: 10.1021/acsanm.2c02533
- [50] P. Senthil Kumar, I. Pastoriza-Santos, B. Rodríguez-González, F. Javier García de Abajo, L.M. Liz-Marzán, *Nanotechnology* 19 (2008) 015606. DOI: 10.1088/0957-4484/19/01/015606
- [51] M.B. Mohamed, K.Z. Ismail, S. Link, M.A. El-Sayed, *J. Phys. Chem. B* 102 (1998) 9370–9374. DOI: 10.1021/jp9831482
- [52] N.R. Jana, L. Gearheart, C.J. Murphy, *Adv. Mater.* 13 (2001) 1389–1393. DOI: 10.1002/1521-4095(200109)13:18<1389::AID-ADMA1389>3.0.CO;2-F
- [53] C.L. Nehl, H. Liao, J.H. Hafner, *Nano Lett.* 6 (2006) 683–688. DOI: 10.1021/nl052409y
- [54] S. Chen, Z.L. Wang, J. Ballato, S.H. Foulger, D.L. Carroll, *J. Am. Chem. Soc.* 125 (2003) 16186–16187. DOI: 10.1021/ja038927x
- [55] M. Schütz, D. Steinigeweg, M. Salehi, K. Kömpe, S. Schlücker, *Chem. Commun.* 47 (2011) 4216. DOI: 10.1039/c0cc05229a
- [56] H. Yuan, C.G. Khoury, H. Hwang, C.M. Wilson, G.A. Grant, T. Vo-Dinh, *Nanotechnology* 23 (2012) 075102. DOI: 10.1088/0957-4484/23/7/075102
- [57] S. Sasidharan, D. Bahadur, R. Srivastava, *RSC Adv.* 6 (2016) 84025–84034. DOI: 10.1039/C6RA11405A
- [58] I. Jung, S. Lee, S. Lee, J. Kim, S. Kwon, H. Kim, S. Park, *Chem. Rev.* 125 (2025) 7321–7388. DOI: 10.1021/acs.chemrev.4c00897
- [59] K. Loza, M. Heggen, M. Eppel, *Adv. Funct. Mater.* 30 (2020). DOI: 10.1002/adfm.201909260
- [60] M. Sankar, N. Dimitratos, P.J. Miedziak, P.P. Wells, C.J. Kiely, G.J. Hutchings, *Chem. Soc. Rev.* 41 (2012) 8099. DOI: 10.1039/c2cs35296f
- [61] N. Blommaerts, H. Vanrompay, S. Nuti, S. Lenaerts, S. Bals, S.W. Verbruggen, *Small* 15 (2019) 1–8. DOI: 10.1002/smll.201902791
- [62] T. Fu, J. Fang, C. Wang, J. Zhao, *J. Mater. Chem. A* 4 (2016) 8803–8811. DOI: 10.1039/C6TA02202B
- [63] A.G.M. da Silva, T.S. Rodrigues, S.J. Haigh, P.H.C. Camargo, *Chem. Commun.* 53 (2017) 7135–7148. DOI: 10.1039/C7CC02352A
- [64] I. Lee, S.W. Han, K. Kim, *Chem. Commun.* 1 (2001) 1782–1783. DOI: 10.1039/b105437f
- [65] A.K. Verma, R.K. Soni, *Opt. Laser Technol.* 163 (2023) 109429. DOI: 10.1016/j.optlastec.2023.109429
- [66] M. Alheshibri, *Nanomaterials* 13 (2023) 2940. DOI: 10.3390/nano13222940
- [67] R. Intartaglia, G. Das, K. Bagga, A. Gopalakrishnan, A. Genovese, M. Povia, E. Di Fabrizio, R. Cingolani, A. Diaspro, F. Brandi, *Phys. Chem. Chem. Phys.* 15 (2013) 3075–3082. DOI: 10.1039/C2CP42656K
- [68] G. Li, Z. Tang, *Nanoscale* 6 (2014) 3995–4011. DOI: 10.1039/C3NR06787D
- [69] P. Rai, *Sustain. Energy Fuels* 3 (2019) 63–91. DOI: 10.1039/C8SE00336j
- [70] R.T. Tom, A.S. Nair, N. Singh, M. Aslam, C.L. Nagendra, R. Philip, K. Vijayamohan, T. Pradeep, *Langmuir* 19 (2003) 3439–3445. DOI: 10.1021/la0266435
- [71] S. Liu, M.D. Regulacio, S.Y. Tee, Y.W. Khin, C.P. Teng, L.D. Koh, G. Guan, M.-Y. Han, *Chem. Rec.* 16 (2016) 1965–1990. DOI: 10.1002/tcr.201600028
- [72] R. Ghosh Chaudhuri, S. Paria, *Chem. Rev.* 112 (2012) 2373–2433. DOI: 10.1021/cr100449n
- [73] R. Purbia, S. Paria, *Nanoscale* 7 (2015) 19789–19873. DOI: 10.1039/C5NR04729C
- [74] Z. Chen, Z.-M. Cui, F. Niu, L. Jiang, W.-G. Song, *Chem. Commun.* 46 (2010) 6524. DOI: 10.1039/c0cc01786h
- [75] Y. Dai, B. Lim, Y. Yang, C.M. Copley, W. Li, E.C. Cho, B. Grayson, P.T. Fanson, C.T. Campbell, Y. Sun, Y. Xia, *Angew. Chemie Int. Ed.* 49 (2010) 8165–8168. DOI: 10.1002/anie.201001839
- [76] M.-H. Jung, Y.J. Yun, M.-J. Chu, M.G. Kang, *Chem. – A Eur. J.*

- 19 (2013) 8543–8549. DOI: 10.1002/chem.201300834
- [77] L.M. Liz-Marzán, A.P. Philipse, J. Colloid Interface Sci. 176 (1995) 459–466. DOI: 10.1006/jcis.1995.9945
- [78] L.M. Liz-Marzán, M. Giersig, P. Mulvaney, Langmuir 12 (1996) 4329–4335. DOI: 10.1021/la9601871
- [79] W. Stöber, A. Fink, E. Bohn, J. Colloid Interface Sci. 26 (1968) 62–69. DOI: 10.1016/0021-9797(68)90272-5
- [80] T. Ung, L.M. Liz-Marzán, P. Mulvaney, Langmuir 14 (1998) 3740–3748. DOI: 10.1021/la980047m
- [81] T. Ung, L.M. Liz-Marzán, P. Mulvaney, J. Phys. Chem. B 103 (1999) 6770–6773. DOI: 10.1021/jp991111r
- [82] P. Mulvaney, M. Giersig, T. Ung, L.M. Liz-Marzán, Adv. Mater. 9 (1997) 570–575. DOI: 10.1002/adma.19970090712
- [83] C. Graf, D.L.J. Vossen, A. Imhof, A. van Blaaderen, Langmuir 19 (2003) 6693–6700. DOI: 10.1021/la0347859
- [84] C. Fernández-López, C. Mateo-Mateo, R.A. Álvarez-Puebla, J. Pérez-Juste, I. Pastoriza-Santos, L.M. Liz-Marzán, Langmuir 25 (2009) 13894–13899. DOI: 10.1021/la9016454
- [85] V. Salgueiriño-Maceira, M.A. Correa-Duarte, M. Spasova, L.M. Liz-Marzán, M. Farle, Adv. Funct. Mater. 16 (2006) 509–514. DOI: 10.1002/adfm.200500565
- [86] I. Pastoriza-Santos, J. Pérez-Juste, L.M. Liz-Marzán, Chem. Mater. 18 (2006) 2465–2467. DOI: 10.1021/cm060293g
- [87] O. Niitsoo, A. Couzis, J. Colloid Interface Sci. 354 (2011) 887–890. DOI: 10.1016/j.jcis.2010.11.013
- [88] C.T. Kresge, M.E. Leonowicz, W.J. Roth, J.C. Vartuli, J.S. Beck, Nature 359 (1992) 710–712. DOI: 10.1038/359710a0
- [89] R.I. Nooney, T. Dhanasekaran, Y. Chen, R. Josephs, A.E. Ostafin, Adv. Mater. 14 (2002) 529–532. DOI: 10.1002/1521-4095(20020404)14:7<529::AID-ADMA529>3.0.CO;2-H
- [90] P. Botella, A. Corma, M.T. Navarro, Chem. Mater. 19 (2007) 1979–1983. DOI: 10.1021/cm0629457
- [91] I. Gorelikov, N. Matsuura, Nano Lett. 8 (2008) 369–373. DOI: 10.1021/nl0727415
- [92] W.-C. Wu, J.B. Tracy, Chem. Mater. 27 (2015) 2888–2894. DOI: 10.1021/cm504764v
- [93] C. Hanske, M.N. Sanz-Ortiz, L.M. Liz-Marzán, Adv. Mater. 30 (2018) 1707003. DOI: 10.1002/adma.201707003
- [94] R.K. Kankala, H. Zhang, C.-G. Liu, K.R. Kanubaddi, C.-H. Lee, S.-B. Wang, W. Cui, H.A. Santos, K. Lin, A.-Z. Chen, Adv. Funct. Mater. 29 (2019) 1902652. DOI: 10.1002/adfm.201902652
- [95] P. Dikshit, J. Kumar, A. Das, S. Sadhu, S. Sharma, S. Singh, P. Gupta, B. Kim, Catalysts 11 (2021) 902. DOI: 10.3390/catal11080902
- [96] S. Ying, Z. Guan, P.C. Ofoegbu, P. Clubb, C. Rico, F. He, J. Hong, Environ. Technol. Innov. 26 (2022) 102336. DOI: 10.1016/j.eti.2022.102336
- [97] S. Swain, S.K. Barik, T. Behera, S.K. Nayak, S.K. Sahoo, S.S. Mishra, P. Swain, Bionanoscience 6 (2016) 205–213. DOI: 10.1007/s12668-016-0208-y
- [98] V. Dhand, L. Soumya, S. Bharadwaj, S. Chakra, D. Bhatt, B. Sreedhar, Mater. Sci. Eng. C 58 (2016) 36–43. DOI: 10.1016/j.msec.2015.08.018
- [99] N. González-Ballesteros, S. Prado-López, J.B. Rodríguez-González, M. Lastra, M.C. Rodríguez-Argüelles, Colloids Surfaces B Biointerfaces 153 (2017) 190–198. DOI: 10.1016/j.colsurfb.2017.02.020
- [100] A. Chahardoli, N. Karimi, A. Fattahi, Adv. Powder Technol. 29 (2018) 202–210. DOI: 10.1016/j.appt.2017.11.003
- [101] T. Ahmad, M. Irfan, S. Bhattacharjee, Procedia Eng. 148 (2016) 1396–1401. DOI: 10.1016/j.proeng.2016.06.558
- [102] M.D. Regulacio, D.-P. Yang, E. Ye, CrystEngComm 22 (2020) 399–411. DOI: 10.1039/C9CE01561B
- [103] R. Rodríguez-Oliveros, R. Paniagua-Domínguez, J.A. Sánchez-Gil, D. Macías, Nanospectroscopy 1 (2016). DOI: 10.1515/nansp-2015-0006
- [104] Y. Xia, D.J. Campbell, J. Chem. Educ. 84 (2007) 91. DOI: 10.1021/ed084p91
- [105] K.E. Fong, L.-Y.L. Yung, Nanoscale 5 (2013) 12043. DOI: 10.1039/c3nr02257a
- [106] B.J. Wiley, S.H. Im, Z.-Y. Li, J. McLellan, A. Siekkinen, Y. Xia, J. Phys. Chem. B 110 (2006) 15666–15675. DOI: 10.1021/jp0608628
- [107] L. Wang, M. Hasanzadeh Kafshgari, M. Meunier, Adv. Funct. Mater. 30 (2020) 2005400. DOI: 10.1002/adfm.202005400
- [108] Antimicrobial Resistance Collaborators. Global burden of bacterial antimicrobial resistance in 2019: a systematic analysis. Lancet. 2022 Feb 12;399(10325):629–655. doi: 10.1016/S0140-6736(21)02724-0. Epub 2022 Jan 19. Erratum in: Lancet. 2022 Oct 1;400(10358):1102. doi: 10.1016/S0140-6736(21)02653-2. PMID: 35065702; PMCID: PMC8841637.

- [109] L.P. Silva, A.P. Silveira, C.C. Bonatto, I.G. Reis, P. V Milreu, in: A. Ficaí, A.M. Grumezescu (Eds.), *Nanostructures Antimicrob. Ther.*, Elsevier, 2017, pp. 577–596. DOI: 10.1016/B978-0-323-46152-8.00026-3
- [110] E. Sánchez-López, D. Gomes, G. Esteruelas, L. Bonilla, A.L. Lopez-Machado, R. Galindo, A. Cano, M. Espina, M. Ettcheto, A. Camins, A.M. Silva, A. Durazzo, A. Santini, M.L. Garcia, E.B. Souto, *Nanomaterials* 10 (2020) 292. DOI: 10.3390/nano10020292
- [111] A.P. Ingle, N. Duran, M. Rai, *Appl. Microbiol. Biotechnol.* 98 (2014) 1001–1009. DOI: 10.1007/s00253-013-5422-8
- [112] A.S. Dove, D.I. Dzurny, W.R. Dees, N. Qin, C.C. Nunez Rodriguez, L.A. Alt, G.L. Ellward, J.A. Best, N.G. Rudawski, K. Fujii, D.M. Czyż, *Front. Microbiol.* 13 (2023). DOI: 10.3389/fmicb.2022.1064095
- [113] R. Vazquez-Muñoz, A. Meza-Villezas, P.G.J. Fournier, E. Soria-Castro, K. Juarez-Moreno, A.L. Gallego-Hernández, N. Bogdanchikova, R. Vazquez-Duhalt, A. Huerta-Saquero, *PLoS One* 14 (2019) e0224904. DOI: 10.1371/journal.pone.0224904
- [114] U.H. Abo-Shama, H. El-Gendy, W.S. Mousa, R.A. Hamouda, W.E. Yousuf, H.F. Hetta, E.E. Abdeen, *Infect. Drug Resist.* Volume 13 (2020) 351–362. DOI: 10.2147/IDR.S234425
- [115] D. Gupta, A. Singh, A.U. Khan, *Nanoscale Res. Lett.* 12 (2017) 454. DOI: 10.1186/s11671-017-2222-6
- [116] M. Smekalova, V. Aragon, A. Panacek, R. Prucek, R. Zboril, L. Kvitek, *Vet. J.* 209 (2016) 174–179. DOI: 10.1016/j.tvjl.2015.10.032
- [117] A. Mohandas, S. Deepthi, R. Biswas, R. Jayakumar, *Bioact. Mater.* 3 (2018) 267–277. DOI: 10.1016/j.bioactmat.2017.11.003
- [118] X. Yang, J. Hou, Y. Tian, J. Zhao, Q. Sun, S. Zhou, *Sci. China Technol. Sci.* 65 (2022) 1000–1010. DOI: 10.1007/s11431-021-1962-x
- [119] G. Benetti, E. Cavaliere, R. Brescia, S. Salassi, R. Ferrando, A. Vantomme, L. Pallecchi, S. Pollini, S. Boncompagni, B. Fortuni, M.J. Van Bael, F. Banfi, L. Gavioli, *Nanoscale* 11 (2019) 1626–1635. DOI: 10.1039/C8NR08375D
- [120] S. Cometa, R. Iatta, M.A. Ricci, C. Ferretti, E. De Giglio, J. *Bioact. Compat. Polym.* 28 (2013) 508–522. DOI: 10.1177/0883911513498960
- [121] A. Elbourne, R.J. Crawford, E.P. Ivanova, J. *Colloid Interface Sci.* 508 (2017) 603–616. DOI: 10.1016/j.jcis.2017.07.021
- [122] G. Mi, D. Shi, M. Wang, T.J. Webster, *Adv. Healthc. Mater.* 7 (2018) 1800103. DOI: 10.1002/adhm.201800103
- [123] M. Liong, B. France, K.A. Bradley, J.I. Zink, *Adv. Mater.* 21 (2009) 1684–1689. DOI: 10.1002/adma.200802646
- [124] Y. Wang, X. Ding, Y. Chen, M. Guo, Y. Zhang, X. Guo, H. Gu, *Biomaterials* 101 (2016) 207–216. DOI: 10.1016/j.biomaterials.2016.06.004
- [125] Q. Liu, Y. Zhang, J. Huang, Z. Xu, X. Li, J. Yang, H. Huang, S. Tang, Y. Chai, J. Lin, C. Yang, J. Liu, S. Lin, J. *Nanobiotechnology* 20 (2022) 386. DOI: 10.1186/s12951-022-01600-9
- [126] S. Patskovsky, E. Bergeron, D. Rioux, M. Simard, M. Meunier, *Analyst* 139 (2014) 5247–5253. DOI: 10.1039/C4AN01063A
- [127] H. Xu, Q. Li, L. Wang, Y. He, J. Shi, B. Tang, C. Fan, *Chem. Soc. Rev.* 43 (2014) 2650. DOI: 10.1039/c3cs60309a
- [128] K. Seekell, M.J. Crow, S. Marinakos, J. Ostrander, A. Chilkoti, W. Adam, J. *Biomed. Opt.* 16 (2011) 116003. DOI: 10.1117/1.3646529
- [129] A. Nsamela Matombi, M. Hasanzadeh Kafshgari, L. Wang, S. Patskovsky, D. Trudel, M. Meunier, *ACS Appl. Nano Mater.* 3 (2020) 4171–4177. DOI: 10.1021/acsanm.0c00376
- [130] Q. Zhan, J. Qian, X. Li, S. He, *Nanotechnology* 21 (2010) 055704. DOI: 10.1088/0957-4484/21/5/055704
- [131] Y. Mantri, J. V Jokerst, *ACS Nano* 14 (2020) 9408–9422. DOI: 10.1021/acsnano.0c05215
- [132] S.G. Alamdari, M. Amini, N. Jalilzadeh, B. Baradaran, R. Mohammadzadeh, A. Mokhtarzadeh, F. Oroojalian, J. *Control. Release* 349 (2022) 269–303. DOI: 10.1016/j.jconrel.2022.06.050
- [133] A.V.P. Kumar, S.K. Dubey, S. Tiwari, A. Puri, S. Hejmady, B. Gorain, P. Kesharwani, *Int. J. Pharm.* 606 (2021) 120848. DOI: 10.1016/j.ijpharm.2021.120848
- [134] Z. Liang, C. Cao, J. Gao, W. Cai, J. Li, D. Wu, Y. Kong, *ACS Appl. Nano Mater.* 5 (2022) 7440–7448. DOI: 10.1021/acsanm.2c01448
- [135] N.T. Ha Lien, A.D. Phan, B.T. Van Khanh, N.T. Thuy, N. Trong Nghia, H.T. My Nhung, T. Hong Nhung, D. Quang Hoa, V. Duong, N. Minh Hue, *ACS Omega* 5 (2020) 20231–20237. DOI: 10.1021/acsomega.0c01939
- [136] Z. Zhang, J. Wang, C. Chen, *Adv. Mater.* 25 (2013) 3869–3880. DOI: 10.1002/adma.201301890
- [137] Z. Lv, S. He, Y. Wang, X. Zhu, *Adv. Healthc. Mater.* 10 (2021) 2001806. DOI: 10.1002/adhm.202001806
- [138] A. Espinosa, J. Reguera, A. Curcio, Á. Muñoz-Noval, C. Kuttner, A. Van de Walle, L.M. Liz-Marzán, C. Wilhelm, *Small* 16

- (2020) 1904960. DOI: 10.1002/sml.201904960
- [139] A. Amirjani, D.F. Haghshenas, *Sensors Actuators B Chem.* 273 (2018) 1768–1779. DOI: 10.1016/j.snb.2018.07.089
- [140] A. Fernández-Lodeiro, J. Fernández-Lodeiro, C. Núñez, R. Bastida, J.L. Capelo, C. Lodeiro, *ChemistryOpen* 2 (2013) 200–207. DOI: 10.1002/open.201300023
- [141] J. Djafari, C. Marinho, T. Santos, G. Igrejas, C. Torres, J.L. Capelo, P. Poeta, C. Lodeiro, J. Fernández-Lodeiro, *ChemistryOpen* 5 (2016) 206–212. DOI: 10.1002/open.201600016
- [142] D. Sahu, N. Sarkar, G. Sahoo, P. Mohapatra, S.K. Swain, *Sensors Actuators B Chem.* 246 (2017) 96–107. DOI: 10.1016/j.snb.2017.01.038
- [143] S. Li, T. Wei, M. Tang, F. Chai, F. Qu, C. Wang, *Sensors Actuators B Chem.* 255 (2018) 1471–1481. DOI: 10.1016/j.snb.2017.08.159
- [144] A. Amirjani, E. Rahbarimehr, *Microchim. Acta* 188 (2021) 57. DOI: 10.1007/s00604-021-04714-3
- [145] A. Minopoli, A. Acunzo, B. Della Ventura, R. Velotta, *Adv. Mater. Interfaces* 9 (2022) 2101133. DOI: 10.1002/admi.202101133
- [146] M. Fleischmann, P.J. Hendra, A.J. McQuillan, *Chem. Phys. Lett.* 26 (1974) 163–166. DOI: 10.1016/0009-2614(74)85388-1
- [147] S. Schlücker, *Angew. Chemie Int. Ed.* 53 (2014) 4756–4795. DOI: 10.1002/anie.201205748
- [148] N. Akkilic, S. Geschwindner, F. Höök, *Biosens. Bioelectron.* 151 (2020) 111944. DOI: 10.1016/j.bios.2019.111944
- [149] A. Sultangazyev, R. Bukasov, *Sens. Bio-Sensing Res.* 30 (2020) 100382. DOI: 10.1016/j.sbsr.2020.100382
- [150] S. Tu, D. Rioux, J. Perreault, D. Brouard, M. Meunier, J. Phys. Chem. C 121 (2017) 8944–8951. DOI: 10.1021/acs.jpcc.6b11954
- [151] M. Haruta, T. Kobayashi, H. Sano, N. Yamada, *Chem. Lett.* 16 (1987) 405–408. DOI: 10.1246/cl.1987.405
- [152] A. Sápi, T. Rajkumar, J. Kiss, Á. Kukovecz, Z. Kónya, G.A. Somorjai, *Catal. Letters* 151 (2021) 2153–2175. DOI: 10.1007/s10562-020-03477-5
- [153] K. An, G.A. Somorjai, *ChemCatChem* 4 (2012) 1512–1524. DOI: 10.1002/cctc.201200229
- [154] Z. Li, S. Ji, Y. Liu, X. Cao, S. Tian, Y. Chen, Z. Niu, Y. Li, *Chem. Rev.* 120 (2020) 623–682. DOI: 10.1021/acs.chemrev.9b00311
- [155] B. Hvolbæk, T.V.W. Janssens, B.S. Clausen, H. Falsig, C.H. Christensen, J.K. Nørskov, *Nano Today* 2 (2007) 14–18. DOI: 10.1016/S1748-0132(07)70113-5
- [156] S. Linic, P. Christopher, H. Xin, A. Marimuthu, *Acc. Chem. Res.* 46 (2013) 1890–1899. DOI: 10.1021/ar3002393
- [157] K.M. Bratlie, H. Lee, K. Komvopoulos, P. Yang, G.A. Somorjai, *Nano Lett.* 7 (2007) 3097–3101. DOI: 10.1021/nl0716000
- [158] C. Gao, F. Lyu, Y. Yin, *Chem. Rev.* 121 (2021) 834–881. DOI: 10.1021/acs.chemrev.0c00237
- [159] T. Zhang, H. Zhao, S. He, K. Liu, H. Liu, Y. Yin, C. Gao, *ACS Nano* 8 (2014) 7297–7304. DOI: 10.1021/nn502349k
- [160] S. Wang, M. Zhang, W. Zhang, *ACS Catal.* 1 (2011) 207–211. DOI: 10.1021/cs1000762
- [161] C. Wang, L. Wang, J. Zhang, H. Wang, J.P. Lewis, F.-S. Xiao, *J. Am. Chem. Soc.* 138 (2016) 7880–7883. DOI: 10.1021/jacs.6b04951
- [162] J. Lee, J.C. Park, J.U. Bang, H. Song, *Chem. Mater.* 20 (2008) 5839–5844. DOI: 10.1021/cm801149w
- [163] A.K. Singh, Q. Xu, *ChemCatChem* 5 (2013) 652–676. DOI: 10.1002/cctc.201200591
- [164] I. Mustieles Marin, J.M. Asensio, B. Chaudret, *ACS Nano* 15 (2021) 3550–3556. DOI: 10.1021/acsnano.0c09744
- [165] L.M. Bronstein, D.M. Chernyshov, I.O. Volkov, M.G. Ezernitskaya, P.M. Valetsky, V.G. Matveeva, E.M. Sulman, *J. Catal.* 196 (2000) 302–314. DOI: 10.1006/jcat.2000.3039
- [166] J. Zhang, G. Chen, D. Guay, M. Chaker, D. Ma, *Nanoscale* 6 (2014) 2125–2130. DOI: 10.1039/C3NR04715F
- [167] F. Godínez-Salomón, M. Hallen-López, O. Solorza-Feria, *Int. J. Hydrogen Energy* 37 (2012) 14902–14910. DOI: 10.1016/j.ijhydene.2012.01.157
- [168] S. Linic, P. Christopher, D.B. Ingram, *Nat. Mater.* 10 (2011) 911–921. DOI: 10.1038/nmat3151
- [169] A. Kumar, P. Choudhary, A. Kumar, P.H.C. Camargo, V. Krishnan, *Small* 18 (2022) 2101638. DOI: 10.1002/sml.202101638
- [170] A. Zaleska-Medynska, M. Marchelek, M. Diak, E. Grabowska, *Adv. Colloid Interface Sci.* 229 (2016) 80–107. DOI: 10.1016/j.cis.2015.12.008
- [171] A. Zielińska-Jurek, E. Kowalska, J.W. Sobczak, W. Lisowski, B. Ohtani, A. Zaleska, *Appl. Catal. B Environ.* 101 (2011) 504–514. DOI: 10.1016/j.apcatb.2010.10.022

- [172] Y. Mizukoshi, K. Sato, T.J. Konno, N. Masahashi, *Appl. Catal. B Environ.* 94 (2010) 248–253. DOI: 10.1016/j.apcatb.2009.11.015
- [173] J.B. Priebe, J. Radnik, A.J.J. Lennox, M.-M. Pohl, M. Karnahl, D. Hollmann, K. Grabow, U. Bentrup, H. Junge, M. Beller, A. Brückner, *ACS Catal.* 5 (2015) 2137–2148. DOI: 10.1021/cs5018375
- [174] K. Qian, B.C. Sweeny, A.C. Johnston-Peck, W. Niu, J.O. Graham, J.S. DuChene, J. Qiu, Y.-C. Wang, M.H. Engelhard, D. Su, E.A. Stach, W.D. Wei, *J. Am. Chem. Soc.* 136 (2014) 9842–9845. DOI: 10.1021/ja504097v
- [175] H. Liang, Q. Meng, X. Wang, H. Zhang, J. Wang, *ACS Appl. Mater. Interfaces* 10 (2018) 14145–14152. DOI: 10.1021/acsaami.8b00677
- [176] J. Nie, A.O.T. Patrocinio, S. Hamid, F. Sieland, J. Sann, S. Xia, D.W. Bahnemann, J. Schneider, *Phys. Chem. Chem. Phys.* 20 (2018) 5264–5273. DOI: 10.1039/C7CP07762A
- [177] S.K. Karuppannan, R. Ramalingam, S.B. Mohamed Khalith, M.J.H. Dowlath, G.I. Darul Raiyaan, K.D. Arunachalam, *Biocatal. Agric. Biotechnol.* 31 (2021) 101904. DOI: 10.1016/j.bcab.2020.101904
- [178] V. Seerangaraj, S. Sathiyavimal, S.N. Shankar, J.G.T. Nandagopal, P. Balashanmugam, F.A. Al-Misned, M. Shanmugavel, P. Senthilkumar, A. Pugazhendhi, *J. Environ. Chem. Eng.* 9 (2021) 105088. DOI: 10.1016/j.jece.2021.105088
- [179] S.A. Anjugam Vandarkuzhali, N. Pugazhenthiran, R. V Mangalaraja, P. Sathishkumar, B. Viswanathan, S. Anandan, *ACS Omega* 3 (2018) 9834–9845. DOI: 10.1021/acsomega.8b01322
- [180] X. Zhu, C. Jin, X.-S. Li, J.-L. Liu, Z.-G. Sun, C. Shi, X. Li, A.-M. Zhu, *ACS Catal.* 7 (2017) 6514–6524. DOI: 10.1021/acscatal.7b01658
- [181] Y. Wang, C. Yang, A. Chen, W. Pu, J. Gong, *Appl. Catal. B Environ.* 251 (2019) 57–65. DOI: 10.1016/j.apcatb.2019.03.056
- [182] J. Low, S. Qiu, D. Xu, C. Jiang, B. Cheng, *Appl. Surf. Sci.* 434 (2018) 423–432. DOI: 10.1016/j.apsusc.2017.10.194
- [183] Y. Lan, Y. Xie, J. Chen, Z. Hu, D. Cui, *Chem. Commun.* 55 (2019) 8068–8071. DOI: 10.1039/C9CC02891A
- [184] D.J. de Aberasturi, A.B. Serrano-Montes, L.M. Liz-Marzán, *Adv. Opt. Mater.* 3 (2015) 602–617. DOI: 10.1002/adom.201500053
- [185] J.-L. Wu, F.-C. Chen, Y.-S. Hsiao, F.-C. Chien, P. Chen, C.-H. Kuo, M.H. Huang, C.-S. Hsu, *ACS Nano* 5 (2011) 959–967. DOI: 10.1021/nn102295p
- [186] H. Choi, J.-P. Lee, S.-J. Ko, J.-W. Jung, H. Park, S. Yoo, O. Park, J.-R. Jeong, S. Park, J.Y. Kim, *Nano Lett.* 13 (2013) 2204–2208. DOI: 10.1021/nl400730z
- [187] S. Chang, Q. Li, X. Xiao, K.Y. Wong, T. Chen, *Energy Environ. Sci.* 5 (2012) 9444. DOI: 10.1039/c2ee22657j
- [188] R. Selvapriya, T. Abhijith, V. Ragavendran, V. Sasirekha, V.S. Reddy, J.M. Pearce, J. Mayandi, J. Alloys Compd. 894 (2022) 162339. DOI: 10.1016/j.jallcom.2021.162339

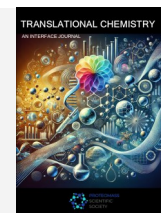
ORIGINAL ARTICLE



TRANSLATIONAL CHEMISTRY

AN INTERFACE JOURNAL

HTTPS://WWW.TRANSLATIONALCHEMISTRY.COM/



ORIGINAL ARTICLE | DOI: 10.5584/translationalchemistry.v1i2.248

Smartphone-based Colorimetric Protein Quantification in Human Urine Using Gold Nanoparticles

Beatriz Quintas^{*,1}, Joana Galhano^{*,1}, Hugo M. Santos^{*,1,2}, Elisabete Oliveira^{*,1,2,3}

¹BIOSCOPE Research Group, LAQV-REQUIMTE, Chemistry Department, NOVA School of Science and Technology, NOVA University of Lisbon, 2829-516, Caparica, Portugal. ²PROTEOMASS Scientific Society, 2825-466, Costa de Caparica, Portugal. ³Canterbury Christ Church University, School of Human and Life Sciences, Life, Sciences Industry, Liaison Lab, Sandwich, UK. ^{*}Both authors contributed equally to this work.

Received: 25 November 2025 Accepted: 27 November 2025 Available Online: 5 December 2025

ABSTRACT

Proteinuria, the presence of elevated protein levels in urine, is an important biomarker associated with various diseases. This study presents a portable, smartphone-based approach for colourimetric protein detection using gold nanoparticles (AuNPs). By inducing the aggregation of AuNPs in the presence of albumin, facilitated by sodium chloride, distinct colour changes were observed and quantified *via* smartphone image analysis. The method was tested using three smartphone models on urine samples from six volunteers, demonstrating a detection limit of 1.19 µg/mL and the ability to visually detect protein concentrations as low as 25 µg/mL. Furthermore, we successfully quantified the urinary proteome of a CRC patient, obtaining a protein concentration of 37 ± 3 µg/mL, which closely agrees with the value of 41 ± 1 µg/mL determined by the Bradford assay. This technique offers a rapid, cost-effective, and non-invasive tool for urinary protein detection, with promising applications in routine clinical diagnostics and disease monitoring.

Keywords: Protein quantification, Proteinuria, Colourimetric detection, RGB analysis, Smartphone-based analysis, Point-of-care testing.

1. Introduction

Proteinuria, characterised by elevated concentrations of protein in the urine, is often associated with an increased risk of renal failure [1,2], along with other health conditions like heart disease, diabetes, and infections [3]. Typically, healthy kidneys filter out less than 150 mg of protein daily, with approximately 20 mg of that being albumin [4]. Protein concentrations in urine ranging from 30 to 300 mg per day are classified as microalbuminuria, while those exceeding 300 mg per day are classified as proteinuria [3]. Additionally, if the daily concentration exceeds 3.5 g of protein, it is categorised as nephrotic range proteinuria. Proteinuria may arise from direct damage to the kidney's glomeruli or from the immune system's response to an infection occurring elsewhere in the body [5]. Frontline protein concentration evaluation in urine is often performed through a urine dipstick analysis. Although it does not require complex sample preparation before analysis as some other methods, it has low sensitivity for lower protein concentrations, for individuals with an albumin/creatinine ratio (ACR) ≥ 30 mg/g, being only recommended as a screening tool in older outpatients with ACR ≥ 300 mg/g [6]. As such, these dipsticks might prove inconclusive for some evaluations with a lower protein concentration.

Other methods can be used for a more accurate protein concentration determination, such as mass spectrometry, immunoassays, fluorescence spectroscopy or Raman spectroscopy. However, these require more extensive sample preparation protocols, are more labour-intensive and time-consuming, and also require expensive equipment [3]. Other colorimetric methods, such as the Bradford assay or the Bicinchoninic Acid (BCA) Assay, can also be used to estimate total protein concentration. However, all these have specific limitations, such as incompatibility with surfactants, a wide range of requirements on needed reagents, or lack of specificity for proteins [7]. Apart from these more conventional methods for protein detection, nanomaterials can also be used to detect protein in urine. Several studies in the literature report protein-nanoparticle interactions, often accompanied by colorimetric alterations and the occurrence of precipitation [8]. Moreover, the formation of a protein corona is also described when protein and nanoparticles dynamically interact with each other, forming hard and soft coronas. These interactions depend on many factors, namely, the surface functionalisation of the nanoparticles, nanoparticle surface charge and size, protein composition, and incubation time [9–12]. The adsorption of different proteins to form a protein corona *via* colorimetric changes was quantitatively

*Corresponding author: Hugo M. Santos and Elisabete Oliveira (hmsantos@fct.unl.pt and ej.oliveira@fct.unl.pt)

characterised by UV-vis absorption spectroscopy [13]. In this assay, four models of proteins were successfully determined with a concentration range of up to 80 µg/mL in water and up to 200 µg/mL in human urine. Moreover, this assay also stands out from conventional commercial protein assays since it allows instantaneous quantification. However, despite being a faster and easier technique, absorption spectroscopy is still necessary for quantification. In recent years, there has been increasing interest in integrating smartphones and image processing programs into chemical analysis, facilitating environmentally friendly, rapid, and cost-effective analytical procedures [14]. Extensive research has been conducted on digital image colourimetry (DIC) as a versatile qualitative and quantitative analysis technique across various sample types, including heavy metals [15], pesticides [16], antibiotics [17], and food products [18]. Despite its versatility, DIC has been underutilised for protein quantification, leaving a significant gap in the research and application of this technique for protein analysis and detection of proteinuria.

Taking advantage of these points, our work sheds light on the development of a more accurate method. Gold nanoparticles (AuNPs) show distinct colours according to the protein-nanoparticle ratios. This allows for a visual determination of albumin in water and protein in urine samples with a minimum concentration of 25 µg/mL. To make the method accessible to everyone, a mathematical model was developed based on the Red-Green-Blue (RGB) characteristics of the colorimetric responses. This model enables the calculation of protein concentration from a simple smartphone image, providing a convenient, fast, and portable solution for protein quantification. As such, the use of nanotechnology combined with DIC methods for protein quantification could bring some advantages for preliminary screenings, not requiring extensive equipment and utilizing a simple sample preparation.

2. Materials and methods

2.1. Chemicals and Starting Materials

Hydrogen tetrachloroaurate (III) trihydrate (99.99%) was purchased from Thermo Scientific. Sodium citrate, tribasic dihydrate (≥ 99%), Bovine Serum Albumin (BSA ≥ 96%) and Bradford reagent were purchased from Sigma-Aldrich. Reagents were used as received.

2.2. Instrumentation

The Nanoparticle size and zeta potential were determined using a Dynamic Light Scattering (DLS) Malvern NanoZetasizer, with a 633 nm laser diode (PROTEOMASS Scientific Society, Caparica, Portugal). UV-Vis absorption spectra were acquired in a Jasco V-650 Spectrophotometer (Jasco Corporation, Tokyo, Japan). 96-well plate readings were performed using a CLARIOSTAR Spectrophotometer (BMG Labtech) (PROTEOMASS Scientific Society Facility). Transmission Electron Microscopy (TEM) images were obtained in a JEOL JEM-2100-HT operating at 200 kV; TEM

images were collected using a "OneView" 4k×4k CCD camera. Photography of the 96-well plates for the RGB assessment assay was taken using smartphones, models OPPO Reno8 Lite, Samsung Galaxy S21 FE 5G and an iPhone 14 Pro. The Simplicity® UV ultrapure water purification system from Merck Millipore was used to produce ultrapure water for all the experiments.

2.3. Gold Nanoparticle Synthesis and Characterization

AuNPs were synthesised according to an already established Turkevich method [19]. Briefly, 4.9 mg of hydrogen tetrachloroaurate (III) was dissolved in 12.5 mL of ultrapure H₂O, and the obtained solution was heated at 100 °C under stirring at 300 rpm. Then, 1.25 mL of a 10 mg/mL sodium citrate aqueous solution was added to the reactional mixture, and it was left under reflux for approximately 15 minutes until a deep red colour was observed. After the colorimetric alteration, the solution was left to cool down to room temperature. Until further use, the obtained nanoparticles were stored as obtained at 4 °C to avoid degradation. The obtained nanoparticles were promptly characterized by acquiring the respective absorption spectrum, and their size and zeta potential were determined through DLS measurements. TEM images were collected to evaluate particle size and morphology.

2.4. Albumin Colorimetric Detection with AuNPs in Aqueous Media

To analyse possible protein interactions with AuNPs the following experiments were conducted and measured by DLS and UV-Vis spectrum: **AuNPs** (1.7 mL H₂O + 300 µL AuNPs + 1.01 mL H₂O); **AuNPs-BSA** (1.7 mL H₂O + 300 µL AuNPs + 10 µL BSA 2 mg/mL + 1 mL H₂O); **AuNPs-BSA-NaCl** (1.7 mL H₂O + 300 µL AuNPs + 10 µL BSA 2 mg/mL + 1 mL NaCl 5 M); **AuNPs-NaCl** (1.7 mL H₂O + 300 µL AuNPs + 10 µL H₂O + 1 mL NaCl 5 M). To further evaluate the system's colorimetric behaviour, a high-throughput miniature set of experiments following similar conditions was performed in a 96-well plate. In a 96-well plate, a gradient concentration of BSA in aqueous solution, ranging from 0 to 97 µg/mL, was prepared with a total volume of 170 µL per well. Next, 30 µL of the synthesised AuNPs were added to each well. Finally, 20 µL of an aqueous 5 M NaCl solution was added to each well. Respective controls, without BSA and NaCl, were also performed under the same conditions.

2.5. Total Protein Colorimetric Detection with AuNPs in Urine Samples

2.5.1. Urine sample collection and treatment

Six urine samples from healthy volunteers and one from a colorectal cancer patient (CRC patient) were collected in sterile collection flasks following informed consent. Before handling, the urine was filtered through a paper filter to remove precipitates. The filtered urine was then diluted 1:20 using ultrapure H₂O and used throughout the study.

2.5.2. Total Protein Colorimetric Detection with AuNPs in Urine Samples

Healthy urine samples were spiked with varying concentrations of BSA (from a stock solution of 2 mg/mL) ranging from 0 to 97 µg/mL. In a 96-well plate, 170 µL of each spiked urine solution and CRC patient urine was added, followed by 30 µL of AuNPs and 20 µL of NaCl. One row of wells without NaCl was used as a negative control to evaluate the response without NaCl.

2.6. Protein Quantification

2.6.1. Total Protein Quantification using Bradford Assay

Total protein quantification of CRC patient urine was performed through a Bradford protein assay [20]. A calibration curve was generated using the following concentrations of BSA stock solutions in ultrapure H₂O: 0, 0.25, 0.5, 1.0 and 1.4 g/L. Five microliters of each stock solution were added to a 96-well plate, followed by 250 µL of the Bradford reagent. Five microliters of each urine sample were also added to the 96-well plate with 250 µL of the Bradford reagent. Each experiment was performed in duplicate. The UV-Vis measurements were conducted at 595 nm.

2.6.1. Protein Quantification using the RGB Method

A calibration curve was obtained by photographic collection of a BSA aqueous gradient in water from 0 to 97 µg/mL in the presence of AuNPs and NaCl in a transparent 96-well plate. Smartphone models used for photographic collection were Samsung Galaxy S21 FE 5G, OPPO Reno 8 Lite and iPhone 14 Pro. After photograph collection, an RGB analysis of each well was conducted with the image software ImageJ. Mean and specific channel values (red channel, green channel, and blue channel) were collected through specific analysis of the respective well and used to calculate the Response value using the following formula [21]:

$$\text{Response (\%)} = 100 \times ([\text{RGB}]_{\text{sample}} - [\text{RGB}]_{\text{mean}}) / ([\text{RGB}]_{\text{mean}} - [\text{RGB}]_{\text{ref}}) (1)$$

Where [RGB]_{sample}: RGB value obtained for the well holding the sample; [RGB]_{mean}: RGB value obtained for the wells without adding

NaCl; [RGB]_{ref} = 255. The obtained Response values were plotted in a linear regression model against log₁₀[BSA] present in each well, yielding the following equation [21]:

$$\text{Response (\%)} = m \log[\text{BSA}] + b (2)$$

Where m: slope of the linear regression curve; b: y-intercept of the obtained linear regression curve. Additionally, the limit of detection (LOD) was also calculated from the following formula [21]:

$$\text{LOD} = 3.3 \times (\sigma/m) (3)$$

Where: σ is the standard deviation of the response and m: slope of the linear regression curve obtained from the previous equation.

3. Optical Properties of Metallic NPs

3.1. AuNPs Synthesis and Characterization

Citrate-capped gold nanoparticles (AuNPs) were synthesised following a well-reported Turkevich method [22]. The obtention of a deep-red characteristic colouration in the reactional mixture indicated a well-achieved AuNPs solution. The obtained nanoparticles were first characterised by UV-Vis spectroscopy and DLS analysis, summarising the results in **Figure 1**. AuNPs present a well-defined absorption profile consistent with those reported in the literature for spherical AuNPs, with a typical plasmonic band appearing at 523 nm. Their hydrodynamic diameter (HD) was 32.5 ± 0.3 nm, with a polydispersity index (PDI) of 0.556 ± 0.002 . The obtained zeta-potential (ζ) was -30.2 ± 0.7 mV, confirming the successful citrate capping of the particles. TEM was also performed to verify the dispersity, size and morphology of the synthesized nanoparticles. The obtained nanoparticles present a well-defined spherical shape with an average diameter of 14 ± 2 nm. These values are in accordance with others reported in the literature for similar particles [22].

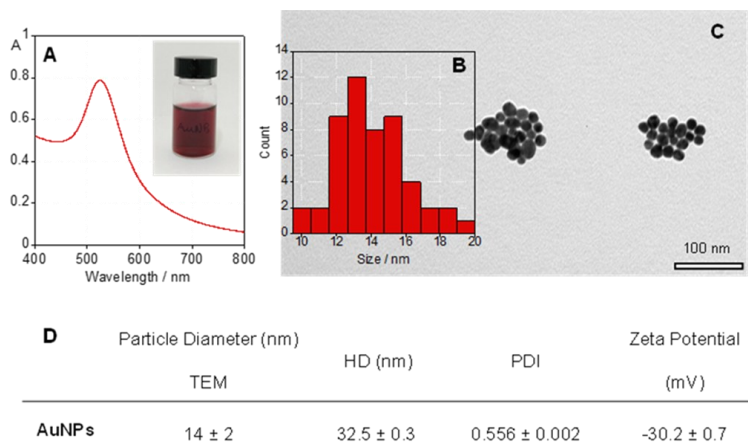


Figure 1. Characterisation of AuNPs: (A) absorption spectra; inset: colourimetric evaluation of the freshly synthesised AuNPs; (B) Size distribution for nanoparticles from TEM analysis; (C) TEM image; and (D) size and particle surface charge of the synthesised nanoparticles.

3.2. AuNPs-Protein Interaction in Aqueous Environments

To evaluate any interactions that might occur between the nanoparticles and protein, AuNPs were diluted with a dilution factor of 0.18 to a total volume of 2 mL, yielding a homogeneous deep-red nanoparticle suspension. Subsequently, 10 μ L of a 2 mg/mL BSA aqueous solution was added to the solution. BSA was selected as a model protein, as albumin is the most prevalent protein in physiological contexts, and the bovine counterpart has similar characteristics to that of the human one. Upon addition of the protein, no colorimetric alterations were verified; however, after the addition of 1 mL of a 5 M NaCl aqueous solution, a substantial colorimetric alteration occurred from red to purple, as seen in **Figure 2**. Upon the addition of NaCl, in the absence of BSA, the nanoparticles lost their deep-red colouration, turning into a clear/

grey solution. At each stage, the absorption spectra were collected, and other properties were analysed through DLS, as summarised in **Figure 2**. BSA was added to the AuNPs suspension to a final concentration of 10 μ g/mL in the cell. Despite this addition, no colorimetric alterations were observed, with the suspension maintaining its characteristic red colouration. However, from analysis of the UV-Vis spectra, a slight alteration of the absorption maximum was observed, with a shift occurring from 523 to 526 nm. This slight redshift is consistent with reports in the literature regarding protein-AuNPs interaction, possibly through the formation of a “protein corona” [23]. A slight alteration in the hydrodynamic diameter obtained for the AuNPs in the presence and absence of BSA was also verified. This alteration can be derived from forming a “soft corona”, meaning the formation of a dynamic layer of protein at the surface of the nanoparticles.

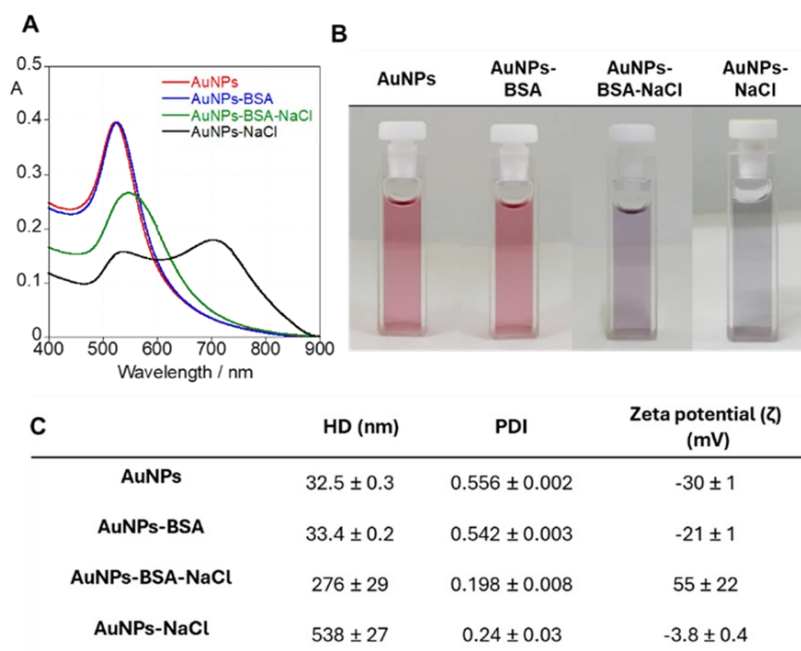


Figure 2. (A) Absorption spectra of free AuNPs (red); AuNPs in the presence of BSA (blue); AuNPs in the presence of BSA and NaCl (green); AuNPs in the presence of NaCl (black). (B) Colourimetric alterations of the tested conditions; (C) Hydrodynamic diameter, polydispersity index and zeta potential of AuNPs in response to the different tested conditions.

This interaction is, however, clearly noticeable from the zeta-potential data obtained for both solutions. Without the addition of BSA, the AuNPs presented a surface charge of ca. -30 mV, a typical charge for citrate-capped AuNPs, due to the negative charge of the citrate moiety [24]. However, upon BSA addition, this charge was altered to ca. -21 mV. This alteration is indicative of BSA-AuNPs surface interactions, partially neutralising the inherent negative surface charge of the nanoparticles. Interestingly, when adding 1 mL of an aqueous solution of NaCl 5 M, drastically increasing the ionic strength of the solution, a colorimetric alteration took place, changing from red to purple hue. Once again, this alteration was accompanied by a visible alteration in the absorption spectra, where the maximum peak suffered a redshift to 547 nm and a decrease in the absorbance intensity, followed by an increase in the hydrodynamic diameter from 33 nm to 276 nm. Such high values

indicate aggregation or clustering phenomena in solution, modulated by the increased ionic strength induced by adding NaCl. Moreover, the zeta-potential measurements indicate a very pronounced charge alteration from the negative values obtained without NaCl. This drastic shift from negative to positive occurring in response to the increased ionic strength of the solution. Several mechanisms might be responsible, however, considering the hydrodynamic diameter values obtained, aggregation phenomena are the most likely to occur. However, another explanation might involve the compression of the electric double layer [25]. This compression could reduce the negative charge available at the surface of the particles, leading to a charge reversal. This effect might also become more pronounced if the free ions in solution adsorb preferentially to the protein corona, particularly Na^+ ions, resulting in a more positive zeta potential.

To best understand the role of NaCl and BSA in these systems, measurements were performed in the same conditions as before, replacing the BSA solution with water. The nanoparticles lost their red colour upon the addition of NaCl, acquiring a clear aspect, with no trace of the purple hue observed in the presence of BSA. Once again, this alteration was accompanied by alterations in the UV-Vis spectra, consistent with other spectra reported in the literature for AuNPs in the presence of increasing NaCl concentrations [24]. Once again, a drastic increase in hydrodynamic diameter was observed, surpassing the values observed for the AuNPs in the presence of BSA and NaCl. These results are once again indicative of the occurrence of aggregation phenomena. Comparing the hydrodynamic diameter measurements obtained for AuNPs-NaCl in the presence and absence of BSA underscores the role of BSA in the AuNPs stabilisation in solution. The presence of BSA appears to help the nanoparticle's stabilisation in the presence of higher ionic strength, although some aggregation persists. Additionally, considering the zeta-potential values obtained for the AuNP-NaCl condition of ca. -3.8 mV, being less negative than those presented by the AuNPs alone but not as positive as the system in the presence of BSA (ca. 55 mV). These differing values might arise due to the absence of a protein corona. As no protein corona exists, fewer Na^+ ions can interact with the negatively charged citrate molecules present on the surface of the particle, thereby neutralizing part of the surface charges available. Under these conditions, the ratio between Na^+ ions and citrate molecules was approximately even, as almost all charges were neutralized. The slight negative charge remaining most likely originates from the citrate molecules that did not interact with the sodium ions in solution.

3.3. High-Throughput Colorimetric Protein Detection in H_2O

Following the above-described assays, the method was scaled down and further optimized for a high-throughput analysis in ultrapure water. Using a 96-well plate as a high-throughput platform, four conditions were prepared, as seen in **Figure 3**. The four conditions tested yielded a clear differential colorimetric profile. Condition 1 combined the AuNPs in a constant concentration with increasing [BSA] ranging from 0 to 97 $\mu\text{g/mL}$ (0, 1, 2, 5, 10, 25, 50, 97 $\mu\text{g/mL}$). Additionally, a constant NaCl concentration was added to each of the wells. Condition 2 consists of the AuNPs in the presence of BSA without the addition of NaCl. Condition 3 consists of the AuNPs in the presence of NaCl without adding BSA. Finally, Condition 4 consists of AuNPs in water without BSA or NaCl. Similarly to what was verified and discussed in the previous section, the presence of BSA in solution, in contact with AuNPs, allows for the formation of a protein corona, which cannot be readily identifiable through a naked-eye assessment from the simple addition of protein to the AuNPs, requiring a revealing agent, which for the purposes of this work was NaCl. By increasing the ionic strength of the solutions, the nanoparticles tended to aggregate, losing their optical properties. This aggregation, associated with a loss of colour, is also verified in Condition 3, in which, in the absence of BSA, the solution went from a red/pink colouration, as seen in Conditions 2 and 4, to a transparent/grey colour verified in Condition 3. As seen in Condition 1, upon adding NaCl to the BSA-AuNPs complex, the wells acquired a gradient of colouration, ranging from a grey/purple hue to the expected red/pink, traditional of the AuNPs. With a lower [BSA], the amount of protein interacting with the AuNPs will be smaller, forming a less defined protein corona.

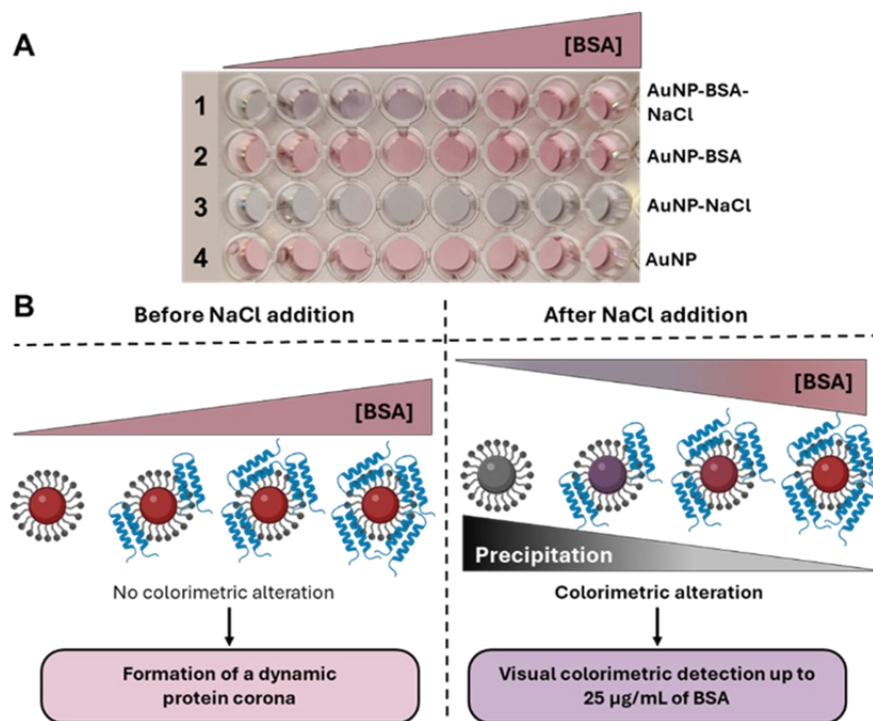


Figure 3. (A) Colourimetric response of AuNPs-BSA solution (with increasing [BSA]), upon NaCl addition in water. (B) Schematic overview of the proposed mechanism of action for AuNP-protein interaction.

With the increase of [BSA], the interactions between protein and nanoparticles will also increase and strengthen the protein corona. Upon the addition of NaCl, the nanoparticles that have the strongest protein corona will not aggregate readily. This precipitation ratio will be inversely proportional to the concentration of BSA in the solution, meaning that the more protein in the solution, the less aggregation and precipitation phenomena will occur. This is also consistent with the observed colorimetric profile. The purple hue appears to be an intermediate state between total aggregation/precipitation and a complete protein corona that protects the nanoparticles and prevents the occurrence of these phenomena.

3.4. AuNPs-Protein Interaction in Human Urine Samples

Following the promising data obtained for scaling down the assay in water, the same methodology was applied to urine samples to assess the method's applicability for protein detection in biological samples. Six different urine samples were collected from healthy volunteers ($n = 6$; 50% male and 50% female). To ensure sample and biological diversity, the urines were collected from healthy individuals with different hydration levels on the same day. The urine samples were first subjected to a simple paper filtration to remove any solid deposits and then diluted in H₂O to a 1:20 ratio. Each diluted urine sample was then spiked with specific volumes of

BSA to ensure a protein gradient of 0 to 97 $\mu\text{g/mL}$. Following this, 170 μL of each spiked urine solution was added to a 96-well plate, followed by the subsequent addition of 30 μL of AuNPs and 20 μL of a 5M NaCl aqueous solution. The same colorimetric gradient was observed, consistent with the results obtained in the water-based assay as seen in **Figure 4**. The solution's colouration shifted from a grey/purple hue to a red/pink hue as the BSA concentration in the solution grew. The BSA concentration range in urine was like the one tested in water, displaying a similar colorimetric behaviour across different samples. To verify the consistency of the assay, various urine samples were evaluated through this method, resulting in colour changes like those observed in water. The first five wells, corresponding to a BSA concentration of 0-10 $\mu\text{g/mL}$, exhibited a purple/grey hue, while wells from the sixth onward remained with the red/pink hue upon NaCl addition. This consistency obtained between the various samples aligns with the proposed mechanism in which, with the increase of BSA in solution, a more stable protein corona forms around the particles, decreasing the precipitation/aggregation phenomena that could occur upon the increase of ionic strength modulated *via* NaCl addition. A similar procedure was performed with the human urine of a patient with colorectal cancer without the addition of BSA. The total protein quantity in the sample was also quantified using Bradford assay.

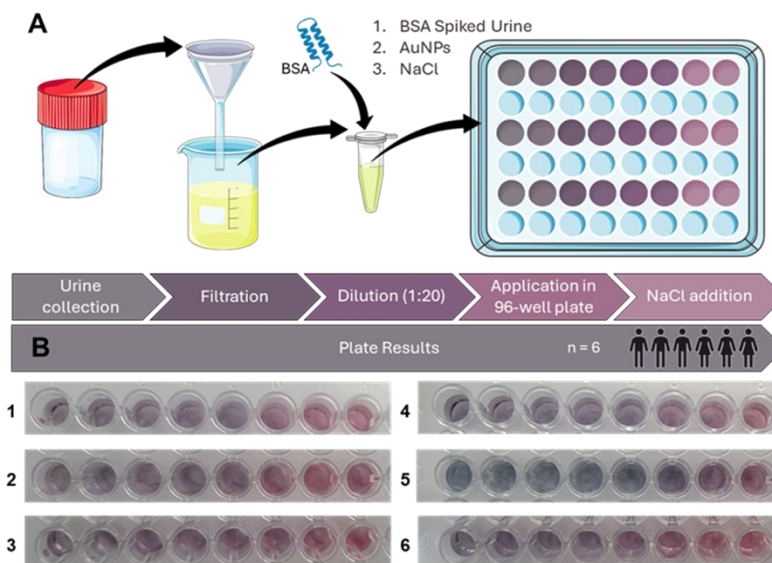


Figure 4. (A) Schematic overview of the urine analysis process, from urine collection and treatment to plate application. (B) Colorimetric response of AuNPs-BSA solution (with increasing [BSA]), upon NaCl addition in urine.

3.5. RGB Smartphone-Assisted Analysis for Protein Quantification

As the method described above allowed for a qualitative determination of protein in solution through a colorimetric alteration, we aimed to develop a quantitative approach for protein quantification in solution, using AuNPs as colorimetric indicators. This approach was based on others already published in the literature, where, through RGB analysis of a photograph, it is possible to quantify a specific analyte that triggers a colorimetric

response on the indicator [21,26,27]. To verify if such an approach was feasible, the first step was to confirm if a linear correlation between the RGB response and the respective BSA concentration in the solution could be obtained. To this end, a BSA gradient in water was performed with the following concentrations: 0, 1, 2, 5, 10, 25, 50, 97 $\mu\text{g/mL}$, in the presence and absence of NaCl, like the above-mentioned assays in water. Images of the plates were captured with a Samsung Galaxy S21 FE 5G smartphone positioned ca. 20 cm above the plate. The plates were photographed under natural light, without direct sunlight irradiation, to prevent reflectance

interference in the 96-well plate. The captured images were then analysed using the free, open-source ImageJ Software [28] to conduct an RGB analysis. A comprehensive colorimetric analysis was performed, obtaining the respective RGB means, as well as the individual Red, Blue and Green Channels for each well. A selection of 5000 pixels, circular area measurement in ImageJ, was performed

in the center part of the wells and all subsequent measurements and colorimetric information was derived from this selection. From here, following a similar approach already reported in the literature, the Response % (R%) was calculated using **Equation 1**, as illustrated in **Figure 5**.

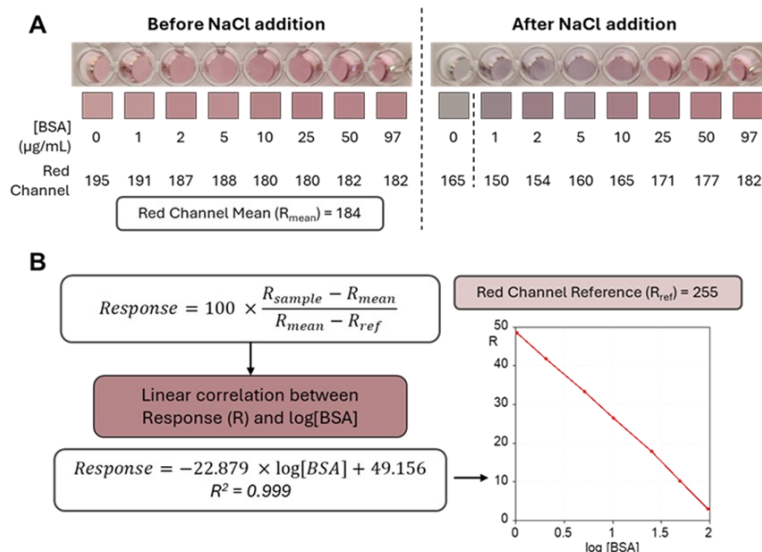


Figure 5. (A) Colorimetric analysis of the water-based calibration curve. (B) Mathematical deduction for Response % calculation and linear correlation between Response % and log [BSA].

This percentage was calculated for all the obtained variations of the RGB analysis: RGB mean, Red Channel mean, Blue Channel mean, and Green Channel mean. The analysis demonstrated that the Red Channel values exhibited the most reliable results, demonstrating a strong linear correlation with protein concentration in solution. In contrast, the blue and green channels had a lower variation in response to the protein gradient and were discarded from further analysis. From here, all further studies were conducted exclusively using the Red Channel mean values. **Figure 5** shows the images obtained, their colorimetric analysis, and their respective mathematical approaches. Using the Red Channel mean values it is possible to calculate the Response (%) and correlate it with the log [BSA] values. A strong linear correlation between these two variables was obtained, demonstrating the feasibility of protein quantification through this method. Moreover, the Limit of Detection (LOD) was also calculated [21] from this dataset, being 1.19 μg/mL, with respect to BSA concentration, a value comparable to other protein quantification methods, as seen in **Table SN1**. From here, we moved on to the evaluation of biological samples under the same conditions as described in the above sections, with respect to the assays involving urine samples. Once again, a constant BSA concentration gradient was maintained in the samples. Plate images were captured with three different smartphone models (Samsung Galaxy S21 FE 5G, OPPO Reno 8 Lite and iPhone 14 Pro) to introduce variation in the analysis and assess the consistency of the method across different camera and smartphone models. Once again, the images were obtained under natural light without direct sun irradiation to avoid the occurrence of reflections in the photograph, at ca. 20 cm from the plate.

The images obtained were evaluated using the ImageJ software, with mean Red Channel values obtained for each condition. After this colorimetric analysis, the recovery percentage was calculated to assess the accuracy of each smartphone model. Additionally, an ANOVA statistical analysis ($n = 6$; $\alpha = 0.05$) was performed to evaluate the potential statistical variance within each smartphone model. The results, as shown in **Table SN2**, indicate that for all models, the p-values were greater than 0.05, suggesting no significant variation in recovery percentages among the individual measurements for each smartphone model. **Table 1** summarises the results obtained for each smartphone model tested. All p-values were $p > 0.05$. The complete recovery data for all BSA concentrations and respective Recovery % values are included in the Supplementary Material. From the previous table's analysis, it becomes clear that the Recovery (%) values were close to 100%, demonstrating the assay's reliability in estimating a quantitative determination of protein in urine in the proposed conditions. Moreover, the statistical ANOVA analysis also demonstrates no significant differences between the smartphone models used, proposing that this method might be used regardless of the smartphone model and camera characteristics used. In addition to these analysis and validation tests, a similar approach was conducted using a urine sample from a patient with colorectal cancer as a preliminary proof of concept for the implementation of this methodology in clinically relevant samples. This sample underwent a parallel assessment through the Bradford assay to allow for a comparative analysis between one of the most employed and established protein quantification methods and the proposed colorimetric method.

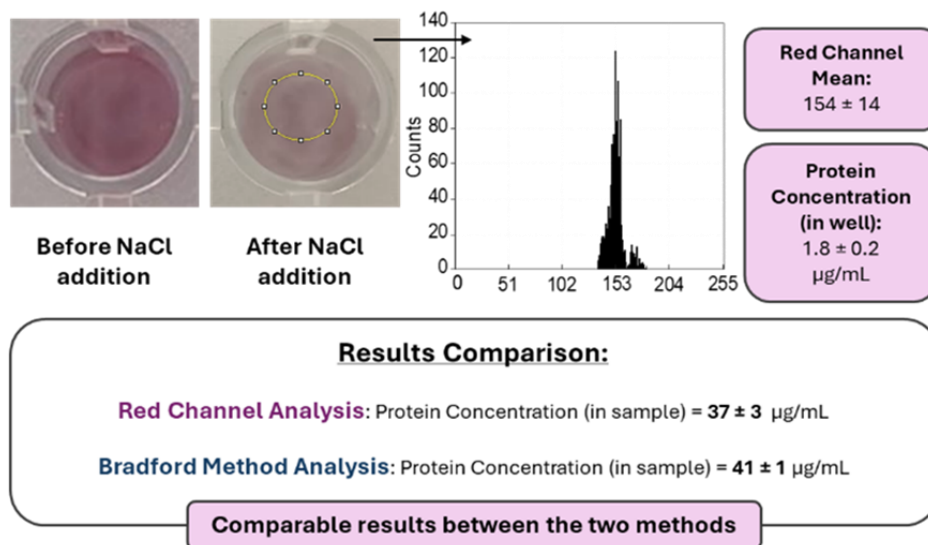
Table 1. Summary of the Response % obtained for each smartphone model.

Smartphone model	Individual	%Recovery \pm Standard Deviation
Samsung Galaxy S21 FE 5G	1	111 \pm 12
	2	105 \pm 14
	3	108 \pm 6
	4	125 \pm 12
	5	105 \pm 17
	6	111 \pm 11
iPhone 14 Pro	1	95 \pm 10
	2	113 \pm 14
	3	112 \pm 11
	4	113 \pm 15
	5	115 \pm 15
	6	109 \pm 10
OPPO Reno 8 Lite	1	104 \pm 9
	2	104 \pm 14
	3	114 \pm 7
	4	109 \pm 10
	5	110 \pm 13
	6	99 \pm 9

Figure 6 summarises the protein quantification results obtained from the two methods. The image was analysed using the ImageJ software, analysing the section highlighted in **Figure 6**.

From these data, we obtained a Response % of 44.59, which translates to a protein concentration of ca. 1.8 ± 0.2 $\mu\text{g/mL}$. Considering the dilution factors, the protein concentration in the urine sample calculated through our method was 37 ± 3 $\mu\text{g/mL}$. In

comparison, Bradford quantification yielded a total protein concentration of ca. 41 ± 1 $\mu\text{g/mL}$. These two values are similar to each other, allowing for the validation of this assay as a powerful tool for protein quantification in urine through a simple, fast and high-throughput method, which relies on a simple photograph analysis obtained *via* a smartphone camera.

**Figure 6.** Summary of the colorimetric analysis of the patient's urine and respective protein quantification results obtained from the Red Channel Analysis and Bradford Method Analysis.

5. Concluding Remarks

In this study, we have demonstrated the feasibility of using gold nanoparticles (AuNPs) for sensitive and specific protein detection, mainly albumin, in urine samples. The interaction between AuNPs and proteins, facilitated by NaCl, induced distinct colorimetric changes that were quantitatively analysed using RGB values obtained from smartphone images. This method showed promising results in visually detecting protein concentrations as low as 25 $\mu\text{g/mL}$ in both aqueous solutions and urine samples. Integrating

smartphone-based RGB analysis further enhances the method's accessibility and usability, enabling the determination of protein with a detection limit of 1.19 $\mu\text{g/mL}$. Moreover, the assay results were also effective for monitoring protein in CRC, where a protein concentration value of 37.17 $\mu\text{g/mL}$ was determined and further validated by the Bradford method. This approach shows great potential for the early detection and monitoring of urinary protein through non-invasive analysis. By offering a rapid, cost-effective, and portable method for protein quantification, our findings may offer a useful tool for monitoring proteinuria in patients.

Supplementary Material

The following supplementary material is available: **Table SN1**: Limits of Detection (LOD) for various techniques for protein detection and quantification; **Table SN2**: Response% data obtained for each smartphone model and each specific condition.

Acknowledgements

This work was financed by national funds from FCT - Fundação para a Ciência e a Tecnologia, I.P., under the scope of the project UID/50006/2023 of the Associate Laboratory for Green Chemistry-LAQV REQUIMTE; as well as the PROTEOMASS Scientific Society (Portugal) for funding support (General Funding Grant 2023–2024). J.G. thanks FCT/MCTES for doctoral support (Grant 2022.09495.BD; <https://doi.org/10.54499/2022.09495.BD>). E.O. thanks Universidade Nova de Lisboa and Fundação para a Ciência e a Tecnologia (FCT) for the Assistant Professor contract granted under the FCT Tenure Programme (2023.11076.TENURE.116). H.M.S. thanks LAQV for his research contract support. We extend our sincere gratitude to Professors C. Lodeiro and J.L. Capelo for their invaluable contributions, particularly in securing funding for state-of-the-art instrumentation at NOVA FCT through collaborative efforts, which have been essential for the success of this research.

Informed Consent Statement

Informed consent was obtained from all subjects involved in the study.

References

- [1] K. Tryggvason, E. Pettersson, Causes and consequences of proteinuria: the kidney filtration barrier and progressive renal failure, *J Intern Med* 254 (2003) 216–224. <https://doi.org/10.1046/J.1365-2796.2003.01207.X>.
- [2] J. Park, D.W. Shin, K. Han, D. Kim, S. Chun, H.R. Jang, Associations Between Kidney Function, Proteinuria, and the Risk of Kidney Cancer: A Nationwide Cohort Study Involving 10 Million Participants, *Am J Epidemiol* 190 (2021) 2042–2052. <https://doi.org/10.1093/aje/kwab140>.
- [3] S. Aitekenov, A. Gaipov, R. Bukasov, Review: Detection and quantification of proteins in human urine, *Talanta* 223 (2021) 121718. <https://doi.org/10.1016/j.talanta.2020.121718>.
- [4] A.S.A. Naderi, R.F. Reilly, Primary Care Approach to Proteinuria, *The Journal of the American Board of Family Medicine* 21 (2008) 569–574. <https://doi.org/10.3122/jabfm.2008.06.070080>.
- [5] J.E. Toblli, P. Bevione, F. Di Gennaro, L. Madalena, G. Cao, M. Angerosa, Understanding the Mechanisms of Proteinuria: Therapeutic Implications, *Int J Nephrol* 2012 (2012) 1–13. <https://doi.org/10.1155/2012/546039>.
- [6] D. Lim, D.-Y. Lee, S.H. Cho, O.Z. Kim, S.W. Cho, S.K. An, H.W. Kim, K.H. Moon, M.H. Lee, B. Kim, Diagnostic accuracy of urine dipstick for proteinuria in older outpatients, *Kidney Res Clin Pract* 33 (2014) 199–203. <https://doi.org/10.1016/j.krcp.2014.10.003>.
- [7] J.G. Song, K.C. Baral, G.-L. Kim, J.-W. Park, S.-H. Seo, D.-H. Kim, D.H. Jung, N.L. Ifekpolugo, H.-K. Han, Quantitative analysis of therapeutic proteins in biological fluids: recent advancement in analytical techniques, *Drug Deliv* 30 (2023). <https://doi.org/10.1080/10717544.2023.2183816>.
- [8] F. Jia, Q. Liu, W. Wei, Z. Chen, Colorimetric sensor assay for discrimination of proteins based on exonuclease I-triggered aggregation of DNA-functionalized gold nanoparticles, *Analyst* 144 (2019) 4865–4870. <https://doi.org/10.1039/C9AN00918C>.
- [9] L. Treuel, G.U. Nienhaus, Toward a molecular understanding of nanoparticle–protein interactions, *Biophys Rev* 4 (2012) 137–147. <https://doi.org/10.1007/s12551-012-0072-0>.
- [10] P. Breznica, R. Koliqi, A. Daka, A review of the current understanding of nanoparticles protein corona composition, *Med Pharm Rep* 93 (2020) 342–350. <https://doi.org/10.15386/mpr-1756>.
- [11] S.R. Saptarshi, A. Duschl, A.L. Lopata, Interaction of nanoparticles with proteins: relation to bio-reactivity of the nanoparticle, *J Nanobiotechnology* 11 (2013) 26. <https://doi.org/10.1186/1477-3155-11-26>.
- [12] G. Bashiri, M.S. Padilla, K.L. Swingle, S.J. Shepherd, M.J. Mitchell, K. Wang, Nanoparticle protein corona: from structure and function to therapeutic targeting, *Lab Chip* 23 (2023) 1432–1466. <https://doi.org/10.1039/D2LC00799A>.
- [13] Y.T. Ho, B. Poinard, E.L.L. Yeo, J.C.Y. Kah, An instantaneous colorimetric protein assay based on spontaneous formation of a protein corona on gold nanoparticles, *Analyst* 140 (2015) 1026–1036. <https://doi.org/10.1039/C4AN01819B>.
- [14] S.H. Elagamy, L. Adly, M.A. Abdel Hamid, Smartphone based colorimetric approach for quantitative determination of uric acid using Image J, *Scientific Reports* 2023 13:1 13 (2023) 1–9. <https://doi.org/10.1038/s41598-023-48962-0>.
- [15] R. Sivakumar, N.Y. Lee, Recent progress in smartphone-based techniques for food safety and the detection of heavy metal ions in environmental water, *Chemosphere* 275 (2021) 130096. <https://doi.org/10.1016/J.CHEMOSPHERE.2021.130096>.
- [16] T. Zhao, X. Liang, X. Guo, X. Yang, J. Guo, X. Zhou, X. Huang, W. Zhang, Y. Wang, Z. Liu, Z. Jiang, H. Zhou, H. Zhou, Smartphone-based colorimetric sensor array using gold nanoparticles for rapid distinguishment of multiple pesticides in real samples, *Food Chem* 404 (2023) 134768. <https://doi.org/10.1016/J.FOODCHEM.2022.134768>.

- [17] F.J. Cao, H.H. Cheng, S.X. Ma, F. Jiao, D.M. Dong, Three-channel smartphone-based aptamer sensor for multiplexed detecting antibiotics in water through resonance light scattering, *Sens Biosensing Res* 38 (2022) 100533. <https://doi.org/10.1016/J.SBSR.2022.100533>.
- [18] B. Peng, J. Zhou, J. Xu, M. Fan, Y. Ma, M. Zhou, T. Li, S. Zhao, A smartphone-based colorimetry after dispersive liquid-liquid microextraction for rapid quantification of calcium in water and food samples, *Microchemical Journal* 149 (2019) 104072. <https://doi.org/10.1016/J.MICROC.2019.104072>.
- [19] J. Turkevich, P.C. Stevenson, J. Hillier, A study of the nucleation and growth processes in the synthesis of colloidal gold, *Discuss Faraday Soc* 11 (1951) 55. <https://doi.org/10.1039/df9511100055>.
- [20] M.M. Bradford, A rapid and sensitive method for the quantitation of microgram quantities of protein utilizing the principle of protein-dye binding, *Anal Biochem* 72 (1976) 248–254. [https://doi.org/10.1016/0003-2697\(76\)90527-3](https://doi.org/10.1016/0003-2697(76)90527-3).
- [21] E. Tan, İ.M. Kahyaoglu, S. Karakuş, A sensitive and smartphone colorimetric assay for the detection of hydrogen peroxide based on antibacterial and antifungal matcha extract silver nanoparticles enriched with polyphenol, *Polymer Bulletin* 79 (2022) 7363–7389. <https://doi.org/10.1007/s00289-021-03857-w>.
- [22] G.A. Marcelo, M.P. Duarte, E. Oliveira, Gold@mesoporous silica nanocarriers for the effective delivery of antibiotics and bypassing of β -lactam resistance, *SN Appl Sci* 2 (2020) 1354. <https://doi.org/10.1007/s42452-020-3023-6>.
- [23] A. Gomes, J.M. Carnerero, A. Jimenez-Ruiz, E. Grueso, R.M. Giraldez-Pérez, R. Prado-Gotor, Lysozyme–AuNPs Interactions: Determination of Binding Free Energy, *Nanomaterials* 11 (2021) 2139. <https://doi.org/10.3390/nano11082139>.
- [24] S. Vijayakumar, S. Ganesan, Preparation and stability of gold nanoparticles, *Indian Journal of Physics* 86 (2012) 989–995. <https://doi.org/10.1007/s12648-012-0161-8>.
- [25] S. Bhattacharjee, DLS and zeta potential – What they are and what they are not?, *Journal of Controlled Release* 235 (2016) 337–351. <https://doi.org/10.1016/j.jconrel.2016.06.017>.
- [26] G. de Carvalho Oliveira, C.C.S. Machado, D.K. Inácio, J.F. da Silveira Petrucci, S.G. Silva, RGB color sensor for colorimetric determinations: Evaluation and quantitative analysis of colored liquid samples, *Talanta* 241 (2022) 123244. <https://doi.org/10.1016/j.talanta.2022.123244>.
- [27] L. Engel, I. Benito-Altamirano, K.R. Tarantik, C. Pannek, M. Dold, J.D. Prades, J. Wöllenstein, Printed sensor labels for colorimetric detection of ammonia, formaldehyde and hydrogen sulfide from the ambient air, *Sens Actuators B Chem* 330 (2021) 129281. <https://doi.org/10.1016/j.snb.2020.129281>.
- [28] C.A. Schneider, W.S. Rasband, K.W. Eliceiri, NIH Image to ImageJ: 25 years of image analysis, *Nat Methods* 9 (2012) 671–675. <https://doi.org/10.1038/nmeth.2089>.